Materials Today Communications 50 (2026) 114537

Contents lists available at ScienceDirect

Materials Today Communications

journal homepage: www.elsevier.com/locate/mtcomm

Phase stability, microstructural evolution, and corrosion behavior of GTAW-welded AISI 316 L austenitic stainless steel

Ricardo Luiz Perez Teixeira [a,*], Allexia Izabella Pinheiro Damasceno [a], Rafael Nascimento [a], Sebastião Bruno Vilas Boas [a], José Carlos de Lacerda [a], Renata Neves Penha [a], Rogério Fernandes Brito [a], Haroldo Lhou Hasegawa [b], Tarcísio Gonçalves de Brito [a], Eduardo Miguel da Silva [c]

[a] *Federal University of Itajuba, Theodomiro Carneiro Santiago Campus, 200 Irmã Ivone Drumond Street, Industrial District II, Itabira, MG 35903-087, Brazil*
[b] *Federal University of Technology – Paraná (UTFPR), Londrina Campus, 731 João Miguel Caram Avenue, 86036-700, Pioneiros, Londrina, PR, Brazil*
[c] *Federal University of São João del-Rei, 170 Frei Orlando Square, Downtown, São João del-Rei, São João del-Rei, MG 36307-352, Brazil*

ARTICLE INFO

Keywords:
AISI 316 L
CALPHAD
GTAW
Phase stability
TC-PRISMA
TCFE7 and TCFE12 thermodynamic databases

ABSTRACT

This work explores the phase changes in welded AISI 316 L stainless steel coated with a nickel-watts bath containing niobium microparticles. The CALPHAD method, using Thermo-Calc with TCFE7, TCFE12, and PRISMA, simulated phase changes during rapid cooling. Simulations identified amounts of austenite, delta ferrite, and a small amount of sigma phase during cooling from 1450 °C to 25 °C. The influence of the Ni-Nb coating on stability and element diffusion was assessed. Results were confirmed by microscopy, microhardness testing, ferritoscopy, and electrochemical testing. The CALPHAD model reliably predicted phase stability, supporting its use in alloy design and in the optimization of welded stainless steel. This study's approach lays the groundwork for the detailed background and motivation discussed in the following introduction.

1. Introduction

AISI 316 L is an austenitic stainless steel alloyed with chromium (Cr), nickel (Ni), and molybdenum (Mo), as shown in Table 1. These elements increase resistance to pitting and crevice corrosion, especially in chloride-rich environments. The low carbon content (<0.03 %) minimizes chromium carbide precipitation at grain boundaries. This preserves resistance to intergranular corrosion after welding [1–5]. However, AISI 316 L is still susceptible to heat during welding. Gas Tungsten Arc Welding (GTAW) introduces high localized heat and thermal gradients. This environment encourages the formation of intermetallic phases such as sigma (σ), chi (χ), and Laves (η) [6–26].

Table 2 presents an example of a Watts bath composition from the literature [28], provided solely to illustrate typical electrolyte formulations used in prior studies [29–35] and not applied in the present experiments. Section 2.4 and Table 3 describe the actual bath composition used in this study, which includes niobium microparticles.

Omit this paragraph; contextual details and distinctions about the actual Watts bath used are sufficiently and more succinctly addressed in the previous paragraph. This keeps the information focused and avoids unnecessary repetition.

A major challenge in welding austenitic stainless steels is maintaining corrosion resistance, which relies on the integrity of a thin chromium-rich passive oxide film. In industrial applications such as chemical processing equipment, offshore structures, biomedical devices, and marine environments, disruption of this passive layer can lead to localized corrosion and premature failure [33,36–39]. Disruption of this film can lead to pitting and stress corrosion cracking [39,40]. Electrochemical techniques, including potentiodynamic polarization, are therefore widely used to assess corrosion behavior and relate microstructural changes induced by welding to functional performance [41–44], which directly links to this study's objectives.

Advances in computational thermodynamics, particularly the CALPHAD approach implemented in Thermo-Calc, have enabled reliable prediction of phase stability and transformation behavior in multicomponent stainless steels subjected to rapid thermal cycles. These models are especially effective in describing the evolution of austenite, δ-ferrite, and σ-phase during welding and post-weld cooling, as widely reported in the literature [16–26,45,46–50]. Based on this scientific background, the present study investigates the influence of a Ni–Nb electroplated

---

* Corresponding author.
E-mail address: ricardo.luiz@unifei.edu.br (R.L.P. Teixeira).

https://doi.org/10.1016/j.mtcomm.2025.114537
Received 6 October 2025; Received in revised form 17 December 2025; Accepted 18 December 2025

coating on the phase stability and corrosion behavior of GTAW-welded AISI 316 L austenitic stainless steel.

CALPHAD models the evolution of austenite, delta-ferrite, and sigma phase, helping interpret changes during welding and post-weld cooling. Simulations clarify the experimental results and reduce trial-and-error in welding design [50–52]. This underscores CALPHAD's value alongside experiments.

Building on these foundations, this study investigates the effect of a nickel–niobium electrodeposited coating on phase stability and microstructural evolution in GTAW-welded AISI 316 L stainless steel. The central hypothesis is that niobium in the nickel coating refines the microstructure and suppresses the formation of harmful phases during rapid thermal cycling in welding. To test this, the study integrates experimental characterization (microscopy, hardness, tensile, and corrosion tests) with CALPHAD-based thermodynamic and kinetic modelling. By combining these approaches, the study develops quantitative correlations between simulations and actual observations. This provides a logical extension of the background to the research implementation.

CALPHAD simulations predicted equilibrium, non-equilibrium, and precipitation phenomena during realistic welding thermal cycles. The results were compared with optical and SEM images, ferrite content from ferritoscopy, and mechanical and corrosion data. This approach links computational predictions of δ-ferrite and σ-phase evolution to observed differences between the HAZ and FZ. It demonstrates the explanatory power of CALPHAD.

Experimental validation included electroplating AISI 316 L with a Ni-Watts bath enriched with niobium particles (<150 μm). GTAW was then performed under Ar + 2 % O_2. The study aimed to evaluate how the Ni–Nb coating affects phase formation, microstructural stability, and corrosion resistance. Characterization used optical/SEM microscopy, ferritoscopy, microhardness testing, and potentiodynamic polarization tests.

The CALPHAD simulations were performed using representative mid-range composition values for AISI 316 L, selected within the ASTM specification limits and consistent with manufacturer data and literature reports [9,27]. This approach accounts for compositional variability associated with different producers and application backgrounds. CALPHAD simulations under equilibrium and Scheil–Gulliver conditions provided quantitative support for the observations in the FZ and HAZ.

The justification for this investigation stems from growing industrial demand for corrosion-resistant and mechanically stable stainless steel. This demand is especially high for structures in chemical plants, oil and gas platforms, biomedical equipment, and marine environments [53–55]. Improving these properties through surface engineering and optimized welding parameters has significant implications for manufacturing, maintenance, and long-term material performance [56–62].

Understanding the interaction between electroplated coatings and the thermal cycles of welding processes is crucial for designing next-generation stainless steel components with tailored performance characteristics [63,64]. Accordingly, this study addresses the following key question: Does niobium in the nickel electroplating layer affect the stability of austenite or ferrite formation during welding? Can surface treatments prevent sigma-phase precipitation or enhance resistance to pitting corrosion? How do these microstructural changes relate to properties such as hardness and tensile strength? These questions frame the approach introduced above.

In summary, this research investigates the microstructural changes and performance of coated and welded AISI 316 L stainless steel. The findings are intended to guide applications of electrochemical coating and welding in advanced stainless steel fabrication. They also contribute to the broader field of materials processing and phase transformation modelling. These outcomes reinforce the connection throughout the introduction between experimental study, thermodynamic modelling, and industrial significance.

Table 2
Properties and bath composition of nickel-Watts solution.

Reagent	Purity (%)	Concentration (mol/L)	Mass (g)	Function
$NiSO_4$	98.0	0.22	118.02	Main Ni ion source
H_3BO_3	99.5	0.13	33.00	pH buffer
$ZnSO_4$	96.0	0.55	330.00	grain refiner / alloying effect
$NiCl_2$	98.0	0.33	106.21	Improves conductivity
Sorbitol	70.0	0.39	134.00	leveling agent/stress reducer

Source: Adapted from [28].

Table 3
Composition of the modified Ni–Watts bath (in $mol·L^{-1}$).

Component	Concentration ($g·L^{-1}$)	Molar Mass ($g·mol^{-1}$)	Concentration ($mol·L^{-1}$)	Function
Ni	240	58.69	≈ 4.09	$NiSO_4$ provides Ni^{2+} ions, and $NiCl_2$ improves conductivity.
Nb	40	92.91	≈ 0.43	Grain refiner/ phase stabilizer
Zn	330	65.38	≈ 5.05	$ZnSO_4$ acts as a grain refiner and Zn dopant, enhancing microstructure and corrosion resistance
Cl^-	45	35.45	≈ 1.27	improves conductivity.
H_3BO_3	30	61.83	≈ 0.49	pH buffer
Sorbitol	134	134	≈ 0.74	leveling agent/ stress reducer

2. Methodology

AISI 316 L austenitic stainless steel was used as the base material. Its chemical composition is provided in [27]. The material meets ASTM F240 (UNS S31603), EN 1.4401, and IMDS ID 336816343 (X2CrNiMo17–12-2) standards. Typical composition by weight is 0.02 % C, 0.44 % Si, 1.33 % Mn, 16.7 % Cr, 10.03 % Ni, 2.02–2.10 % Mo, 0.032 % P, 0.001 % S, and 0.03 % N. Sheets from Aperam South America measured 282 mm × 210 mm × 4 mm. The material was cold-rolled to a 30 ± 1 % thickness reduction, then annealed at 1050 ± 5 °C for 30 min in an air furnace. Samples were pickled in a nitric–hydrofluoric acid solution (20 % HNO_3 and 5 % HF by volume) for 15 min, following ASTM A380 protocols [65]. This process reduced internal stress and optimized surface conditions for further processing.

Table 1
Chemical composition of AISI 316 L stainless steel.

Element	C	Si	Mn	P	S	Cr	Ni	Mo	N
wt%	≤ 0.03	≤ 0.75	≤ 2.00	≤ 0.045	≤ 0.030	16.0 – 18.0	10.0 – 14.0	2.0 – 3.0	≤ 0.10

Source: Adapted from [27].

2.1. Experimental procedures (Brief overview)

To validate the simulations, welded joints were produced by GTAW using Ar + 2 % O_2. Electroplating was carried out in a modified Watts bath containing 10 g Nb particles per 250 mL. Fig. 1 summarizes the complete experimental and computational workflow adopted in this study, including sample preparation, electroplating, welding, microstructural and mechanical characterization, electrochemical testing, and CALPHAD simulations. Optical microscopy, SEM/EDS, ferritoscopy, Vickers microhardness, and potentiodynamic polarization tests were performed to correlate the experimental data with the CALPHAD predictions for the FZ and HAZ regions.

Fig. 1 provides a clear overview of the methodological sequence adopted in this study. The complete experimental workflow is summarized as follows: sample preparation → Ni–Nb composite electroplating → GTAW welding of the coated specimens → optical and SEM-based microstructural characterization → ferritoscopy for δ-ferrite quantification → Vickers microhardness profiling across the weld → tensile testing of BM, HAZ, and FZ samples → potentiodynamic corrosion evaluation → and CALPHAD thermodynamic and kinetic simulations.

This sequence reflects the logical progression from material preparation and welding to mechanical, microstructural, and electrochemical characterization, concluding with computational thermodynamic analysis to correlate experimental findings with predicted phase stability.

2.2. Sample preparation

Sample preparation begins with wire electrical discharge machining (EDM) on a EUROSTEC EURO FW2 machine using a molybdenum wire (Ø = 0.18 mm) sourced from Eroma EDM. Two plates of approximate size 181 mm × 210 mm × 4 mm are extracted. This non-contact thermal process minimizes residual stress and dimensional deviations.

Surface preparation for coating involves grinding with SiC papers of up to P1200 grit (sandpaper grading according to the Federation of European Producers of Abrasives - FEPA), followed by ultrasonic cleaning in acetone and ethanol baths. The procedure at room temperature removes oxides and contaminants that could inhibit coating adhesion.

2.3. Electroplating of Ni-Nb composite layer

Nickel electroplating, illustrated in Fig. 2, employed a Watts-type bath adapted from Ref. [66], enriched with 10 g Nb particles (<150 µm) per 250 mL. The standard composition was 240 g L^{-1} $NiSO_4·6H_2O$, 45 g L^{-1} $NiCl_2·6H_2O$, and 30 g L^{-1} H_3BO_3. Table 3 lists the bath composition converted to mol L^{-1} for consistency. Niobium particles were kept suspended by magnetic stirring (300 rpm). The bath pH was maintained at 4.0 ± 0.1 using diluted H_2SO_4 and NaOH. The deposition was conducted at room temperature for 20 min under a current density of 2 A dm^{-2}. This specific composite electrodeposition process, as shown in Table 3, produced a uniform Ni-W-Nb layer (~2–3 µm) in thickness, as verified by profilometry (Fig. 2).

A pure nickel anode is employed to ensure consistent replenishment of metal ions in the electrolyte. The cathodic and current efficiencies are calculated using Faraday’s law, yielding a current efficiency of approximately 0.69 for a deposited thickness of 3 µm [67–69]. The coatings are subsequently rinsed with distilled water and dried under hot air.

Composite electrodeposition techniques, such as this one, are employed to enhance the surface properties of stainless steels, including microhardness, wear resistance, and corrosion behavior [70,71].

2.4. GTAW welding

The tungsten inert gas welding (GTAW) process is performed with a constant-current DC power source [72–74]. Pure argon (Ar) with 2 % oxygen (O_2) is used as the shielding gas, delivered at a flow rate of 12 L/min. The filler material is ER316L, and the process parameters are 120 A, 13 V, and 3 mm/s.

The welding equipment used in this study is shown in Fig. 3(A). In

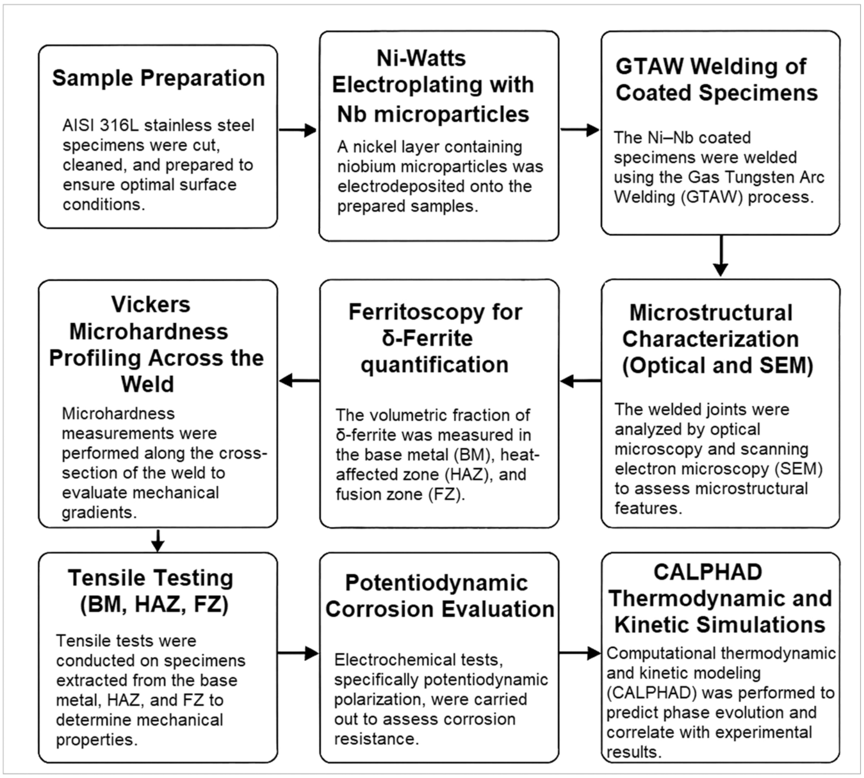

AISI 316L stainless steel specimens were cut, cleaned, and prepared to ensure optimal surface conditions.

A nickel layer containing niobium microparticles was electrodeposited onto the prepared samples.

The Ni–Nb coated specimens were welded using the Gas Tungsten Arc Welding (GTAW) process.

The welded joints were analyzed by optical microscopy and scanning electron microscopy (SEM) to assess microstructural features.

The volumetric fraction of δ-ferrite was measured in the base metal (BM), heat-affected zone (HAZ), and fusion zone (FZ).

Microhardness measurements were performed along the cross-section of the weld to evaluate mechanical gradients.

Tensile tests were conducted on specimens extracted from the base metal, HAZ, and FZ to determine mechanical properties.

Electrochemical tests, specifically potentiodynamic polarization, were carried out to assess corrosion resistance.

Computational thermodynamic and kinetic modeling (CALPHAD) was performed to predict phase evolution and correlate with experimental results.

Fig. 1. Summary of the experimental and computational workflow.

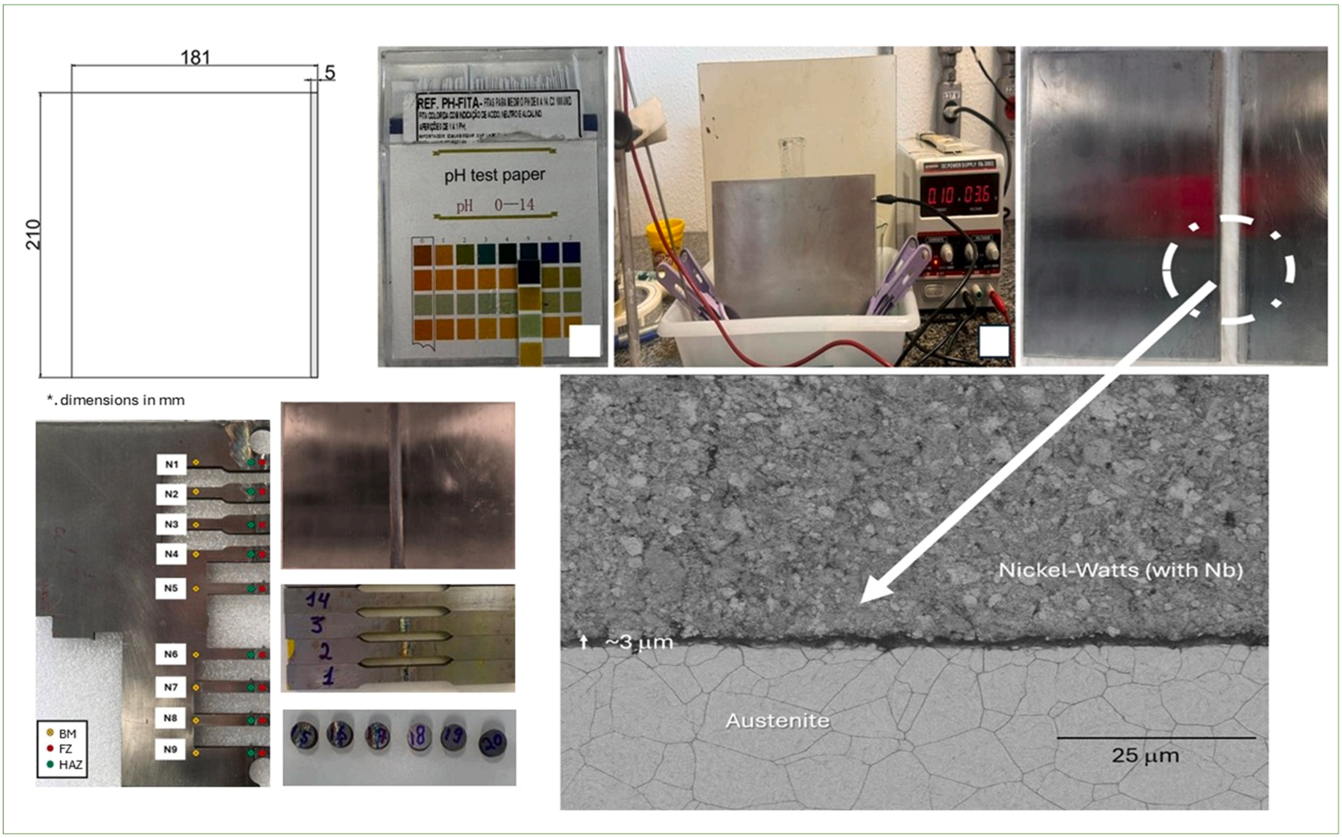

Fig. 2. Electroplated Ni–Watts–Nb layer on AISI 316 L.

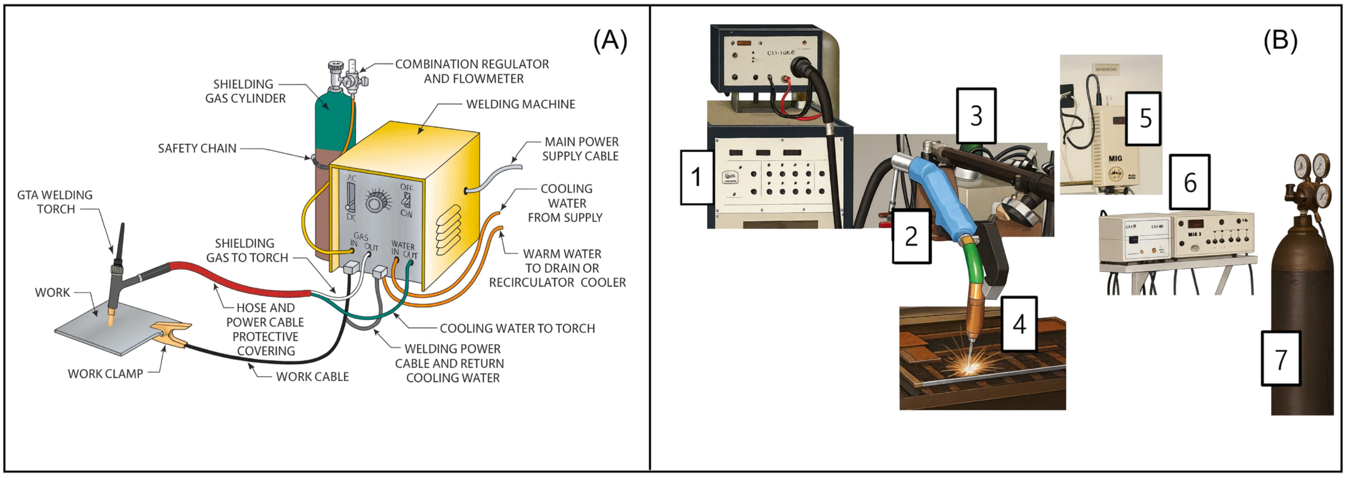

Fig. 3. GTAW welding setup: (A) schematic; (B) equipment details.

contrast, Fig. 3(B) provides a detailed view of the welding setup, including the Inversal 300 multi-process power supply, equipped with digital control and operated in current-controlled mode for pulsed transfer (1), maintaining a constant welding voltage during the tests. The welding torch (2) was mounted on an MC-46 welding carriage, ensuring a stable, controlled travel speed during flat-position welding (3). For specimen fixation and weld-root protection, a system with movable fasteners (4) attached to a support bracket was employed to introduce an inert backing gas (argon) at a controlled flow rate. The length of filler wire consumed in each test, as well as the welding time, was monitored using a tachometer coupled to a wire-feed speed meter (MVA-1) (5). The shielding gas (7) flow rate was kept constant throughout the welding procedure and was monitored using the VGA flowmeter (6).

To ensure reproducibility and facilitate comparison with similar welding studies, all Gas Tungsten Arc Welding (GTAW) parameters used in this work are summarized in Table 4. The welding conditions were kept constant throughout the experimental procedure to minimize thermal variability and ensure consistent heat input, shielding environment, and arc stability. These parameters directly influence solidification behavior, δ-ferrite formation, and the microstructural gradients analyzed in the fusion zone (FZ) and heat-affected zone (HAZ). They are therefore essential for interpreting the mechanical and electrochemical results presented in this study.

Table 4
GTAW welding parameters.

Parameter	Value
Current	120 A
Voltage	13 V
Travel speed	3 mm/s
Shielding gas	Ar + 2 % O_2
Gas flow rate	12 L/min
Torch angle	70°
Arc length	2 mm

Welding is performed manually with a torch angle of 70° and an arc length of approximately 2 mm. The pre-weld and post-weld regions are cleaned with stainless steel brushes to remove oxides and residues that may compromise joint integrity.

To improve the transparency and reproducibility of the mechanical testing procedures, Fig. 4 illustrates the welded plate and the extraction layout for all specimens. Fig. 4(A) identifies the regions from which each tensile specimen (BM, HAZ, and FZ) was sectioned, as well as the transverse path used for microhardness measurements across the joint. The sampling map in Fig. 4(B) also shows the exact orientation and spacing of the gauge sections relative to the weld bead, along with the cut-off locations for the specimens described in Sections 2.5 and 2.6, ensuring consistent representation of the thermal gradients in the fusion and heat-affected zones. This visual guide complements the description of Sections 2.5 and 2.6 by providing a clear overview of specimen positioning, enabling accurate interpretation of the mechanical and microstructural results.

2.5. Tensile testing

Tensile tests were conducted according to ASTM E8/E8M-21 [75] using a universal testing machine (Instron 3369) at room temperature. The strain rate was maintained at 1 mm/min until fracture. The dimensions of the test specimens conformed to standard sub-size flat specimens (gauge length: 25 mm, width: 6 mm, thickness: 3 mm). A total of nine specimens were tested: three from the base metal (BM), three from the fusion zone (FZ), and three from the heat-affected zone (HAZ). This distribution allowed independent statistical analysis of each region’s mechanical response.

2.6. Microhardness testing

Vickers microhardness measurements are performed using a Shimadzu HMV-G20 microhardness tester with a load of 500 gf and a dwell time of 15 s at room temperature [76]. Measurements are taken across the cross-section of welded joints at 0.2 mm intervals to capture hardness gradients from BM to HAZ and FZ. Five indentations per region are averaged for consistency.

This method is suitable for assessing the mechanical changes induced by thermal cycles during welding, as suggested in prior studies on stainless steel joints [77,78].

2.7. Ferritoscopy

Ferrite content is measured using a Fischer Feritscope MP30 [79,80], which detects ferromagnetic phases by measuring changes in magnetic permeability. The induced voltage is proportional to the volume fraction of ferromagnetic constituents such as delta ferrite. This non-destructive method provides quantitative data on the volumetric fraction of ferromagnetic phases, such as delta ferrite (δ-ferrite) and Fe-rich carbides. Measurements are taken from the cross-section in the FZ and HAZ regions to investigate solidification and phase transformation patterns. The method is calibrated using certified standards per ASTM E562 [81]. Five measurements were taken per region (BM, HAZ, FZ) and averaged for statistical consistency.

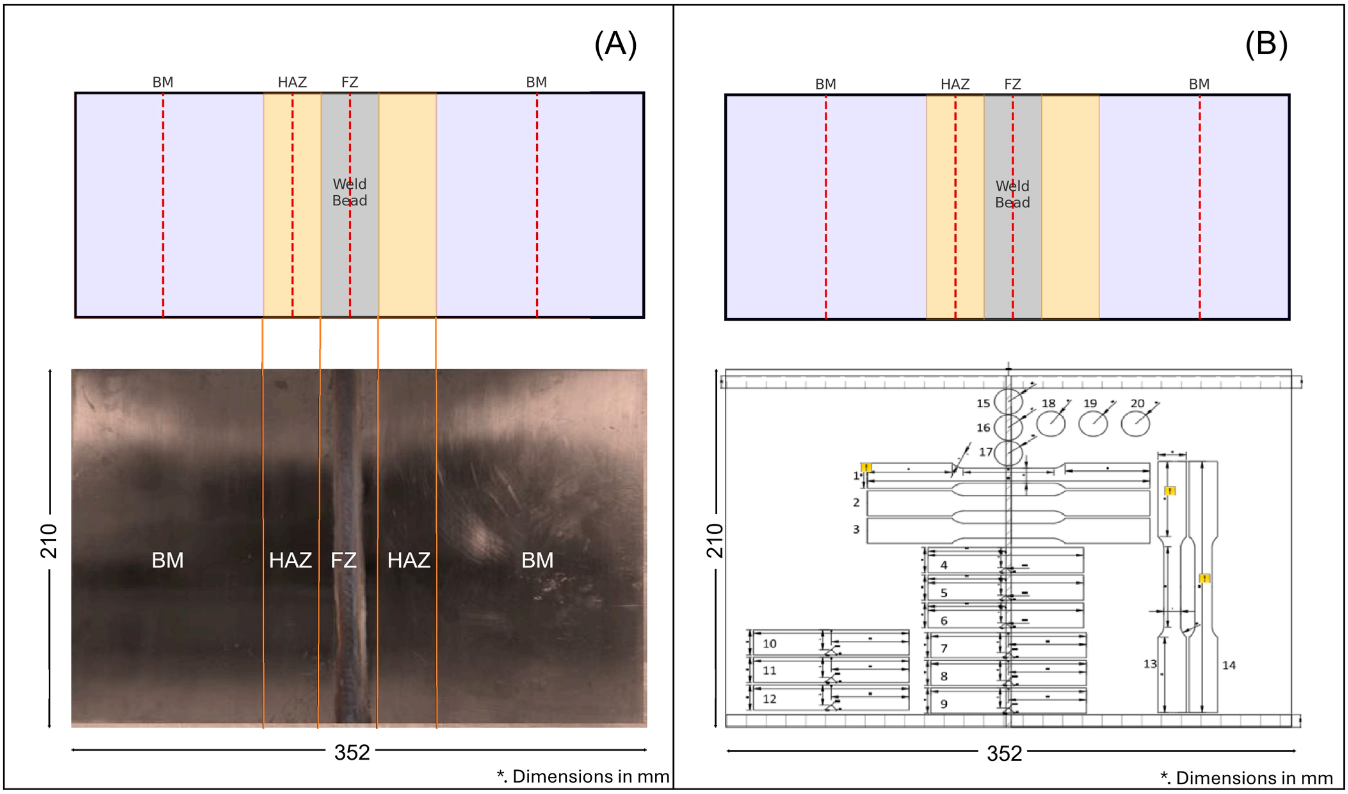

Fig. 4. Extraction scheme for mechanical testing: (A) regions used for tensile and microhardness sampling; (B) orientation and spacing of gauge sections and cut-off locations across the welded joint.

2.8. *Potentiodynamic polarization*

Electrochemical behavior is evaluated by potentiodynamic polarization in a three-electrode cell, using a saturated calomel electrode (SCE) as the reference, a platinum mesh as the counter electrode, and the sample as the working electrode. The test solution is 3.5 % NaCl, maintained at 25 ± 2 °C. The open-circuit potential is stabilized for 60 min before a scan rate of 1 mV/s is applied over the range of –0.25 to + 1.0 V versus OCP.

The corrosion potential (Ecorr), corrosion current density (Icorr), and pitting potential (Epit) are derived from Tafel extrapolation. The tests conform to ASTM G5 and G59 standards [82,83].

Electrochemical methods, such as these, are commonly employed to assess corrosion resistance in welded and coated stainless steels [80,84,85]. The exposed working area was 1.0 cm^2 (100 mm^2) and was defined using an epoxy resin mask.

2.9. *Optical microscopy and SEM*

Metallographic specimens are prepared by standard grinding and polishing, followed by etching with Glyceregia (a mixture of 15 mL HCl, 10 mL glycerol, and 5 mL HNO_3). Microstructures are examined using an Olympus BX53M optical microscope.

Further investigation is performed using a scanning electron microscope (SEM) ZEISS EVO MA10 equipped with energy-dispersive X-ray spectroscopy (EDS) to identify chemical compositions and morphologies. The SEM operates at an accelerating voltage of 20 kV, with a working distance of 10 mm.

These analyses enable the identification of features such as dendritic structures, inclusions, grain boundaries, and precipitates, which play significant roles in defining mechanical and corrosion behavior [45,46,86]

2.10. *Thermodynamic modeling*

Phase stability and precipitation behavior are simulated using Thermocalc Software version 2024b [87]. The CALPHAD (Calculation of Phase Diagrams) method is employed to calculate phase equilibria and transformation kinetics using the TCFE7 and TCFE12 thermodynamic databases, along with the DICTRA and TC-PRISMA modules.

CALPHAD enables the calculation of Gibbs free energy, solvus curves, driving forces, and Pourbaix diagrams for various conditions. Simulation outputs are cross-validated against experimental microscopy and electrochemical tests [47,88,89].

To evaluate the phase transformation behavior of AISI 316 L stainless steel under non-equilibrium cooling conditions, thermodynamic simulations were conducted using CALPHAD methodology. The calculations were based on the nominal chemical composition of the alloy, as outlined in Table 1, using representative mid-range values within the compositional limits specified by ASTM standards. It is essential to note that CALPHAD simulations were conducted based on the bulk 316 L composition and did not account for the effects of the Nb-rich coating, given the limited diffusion observed during welding.

The thermodynamic simulations, using the CALPHAD methodology, were conducted with Thermo-Calc Software (version 2024b) to evaluate phase stability and transformation behavior under thermal conditions relevant to welding [87]. For these simulations, we employed the TCFE7 and TCFE12 thermodynamic databases for both equilibrium and non-equilibrium calculations, alongside the MOBFE5 mobility database for kinetic analyses. TCFE7 was used to maintain consistency with earlier datasets on 316 L stainless steel, which are commonly reported in the literature. In contrast, TCFE12 incorporates updated Cr–Ni–Mo interaction parameters, thereby improving accuracy for multicomponent stainless-steel systems.

The final predictions for phase stability presented in this study were primarily derived from TCFE12, and a cross-comparison with the TCFE7 database confirmed consistent trends in the evolution of δ-ferrite and the formation of σ-phase. The simulations successfully replicated continuous cooling from 1450 °C to 25 °C using both equilibrium thermodynamics and the Scheil–Gulliver non-equilibrium solidification models. Additionally, the TC-PRISMA module was utilized to estimate the nucleation and growth behavior of secondary phases, such as metallic carbides.

The primary phases monitored during the cooling process included delta ferrite (δ), austenite (γ), and the sigma phase (σ). The evolution of phase fractions was plotted as a function of temperature to represent the transformation kinetics and the phase stability ranges. The data were post-processed and visualized in Python using Matplotlib to reproduce the graphical style commonly used in CALPHAD output, enabling clear interpretation of the temperature ranges associated with each transformation.

For the TC-PRISMA simulations, the following parameters were assumed: an average initial grain size of 10 µm, an interfacial energy of 0.5 J/m^2 for $M_{23}C_6$ carbides, and a molar volume of 7.1 × 10^{-6} m^3 /mol. These values are consistent with literature data for austenitic stainless steels and were used to estimate nucleation rates and precipitate growth during continuous cooling [71,90,91].

The simulations were performed using Thermo-Calc Software v. 2024b with the TC-PRISMA module, considering the nominal chemical composition of AISI 316 L stainless steel. The imposed cooling rate (≈ 40°C·s) corresponds to the typical thermal gradients in GTAW. For TC-PRISMA, an initial grain size of 10 µm, an interfacial energy of 0.5 J m^{-2} for $M_{23}C_6$ carbides, and a molar volume of 7.1 × 10^{-6} m^3 mol^{-1} were adopted, consistent with the literature for austenitic stainless steels [90–92].

This methodology provides a reliable framework for predicting microstructural evolution in austenitic stainless steels subjected to high cooling rates, thereby supporting the design and interpretation of heat treatment and welding procedures.

3. Results and discussion

3.1. *Thermodynamic modeling*

Fig. 5 shows the calculated evolution of phase fractions for AISI 316 L stainless steel, cooled continuously from 1450 °C to 25 °C at 40 °C·s under non-equilibrium conditions. The temperature axis (25–1500 °C) covers the stability fields of the main phases. The results, integrated with the TC-PRISMA module, employed literature-derived parameters to estimate nucleation rates, growth kinetics, and precipitate size distributions. Post-processing in Python (Matplotlib [93]) generated phase-fraction curves, indicating that γ-austenite rapidly forms and

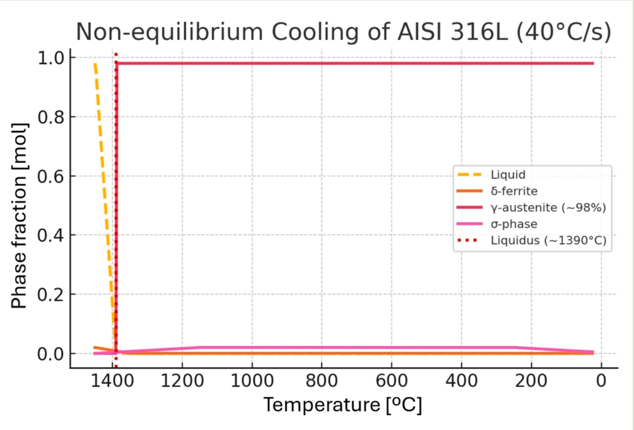

Fig. 5. Non-equilibrium phase evolution of AISI 316 L during rapid cooling (40°C·s^{-1}).

dominates (~98 %) during cooling, while δ-ferrite appears only transiently at the onset of solidification. σ-phase and $M_{23}C_6$ carbides nucleate at lower temperatures in trace amounts. This workflow integrates thermodynamic, kinetic, and precipitation modelling to construct a transformation map relevant to rapid solidification and welding conditions.

Using the TCFE12 thermodynamic and MOBFE5 mobility databases, the simulation incorporated kinetic effects through the Scheil–Gulliver approximation. The alloy remains fully liquid at 1450 °C and begins solidification near 1390 °C. A minor δ-ferrite fraction forms transiently before being replaced by γ-austenite, which becomes dominant (~98 %) for the remainder of the cooling cycle. The CALPHAD-predicted δ-ferrite fraction around 5 % (≈ 0.05 phase fraction mol) matches the ferritoscopy measurements in the fusion zone (6.7 %), confirming the accuracy of the non-equilibrium model. The predominance of γ is typical of rapid solidification, as high cooling rates suppress equilibrium transformations. Only trace amounts of σ-phase precipitates form at low temperatures because limited diffusion hinders their growth.

The slightly higher δ-ferrite fraction measured experimentally may explain the minor reduction in ductility and the increased corrosion current observed later in the FZ. According to CALPHAD predictions, δ-ferrite promotes chromium-rich segregation at interdendritic boundaries, locally reducing the pitting potential and linking phase stability to the mechanical and electrochemical behaviour of welded joints.

For clarity, phases known to be kinetically inhibited during rapid solidification, such as the G-phase, were rejected from the Scheil–Gulliver calculations to avoid unrealistic underestimation of the solidus temperature. Although the precipitation kinetics were not plotted on a logarithmic scale, the TC-PRISMA output confirmed that the nucleation rate of $M_{23}C_6$ carbides sharply increases below 800 °C. Additionally, microsegregation effects are inherently accounted for within the non-equilibrium framework and are expected to be most significant in the fusion zone, where rapid cooling limits solute redistribution.

The chromium and nickel equivalents (Creq and Nieq) for the base metal were calculated from the alloy’s nominal composition following Eqs. (1) and (2). These values provide the basis for correlating phase-field predictions from CALPHAD with the ferrite content measured experimentally by ferritoscopy. Table 5 presents the calculated values of Nieq (Eq. 1) and Creq (Eq. 2) for the base metal (BM), based on its chemical composition and considering the typical values for AISI 316 L stainless steel provided by the manufacturer Aperam [27].

The chromium equivalent in Table 5 is calculated using the formula [94]:

$$\mathrm{Creq} = \%\mathrm{Cr} + \%\mathrm{Mo} + 1.5\times\ \%\mathrm{Si} + 0.5\times\ \%\mathrm{Nb} \tag{1}$$

The nickel equivalent in Table 5is calculated using the formula:

$$\mathrm{Nieq} = \%\mathrm{Ni} + 30\times\ \%\mathrm{C} + 0.5\times\ \%\mathrm{Mn} + 30\times\ \%\mathrm{N} \tag{2}$$

Fig. 6 presents the Schaeffler-DeLong diagram, which predicts phase stability based on chromium and nickel equivalents. The Schaeffler-Delong diagram is a crucial tool for estimating the microstructural composition of the weld fusion zone. To apply it, calculate the chromium equivalent (Creq) and the nickel equivalent (Nieq). This diagram allows the estimation of the expected microstructural balance in the fusion zone and supports the CALPHAD predictions of δ-ferrite formation. Creq and Nieq values were determined as described in Eqs. (1) and (2) to enable this comparison. The Schaeffler–DeLong diagram places the nominal composition of AISI 316 L within the fully austenitic field, exhibiting only a minor tendency to δ-ferrite formation, in agreement with literature reports for this alloy [1,3,13,27].

The Scheil-Gulliver model simulation for AISI 316 L shows the non-equilibrium solidification path, where the solid fraction gradually increases as temperature decreases, starting from a fully liquid phase and progressing through the formation of primary austenite/ferrite and subsequent precipitation of intermetallic compounds (G-phase, M_5SI_3, M_6C, M_7C_3), silicides (CR_3SI, SIC), and carbides. This behavior, illustrated in Fig. 7, reveals a prolonged solidification range and distinct phase transformation steps due to microsegregation effects, highlighting the sequential emergence of phases and their corresponding solid fractions.

While both the Schaeffler-DeLong diagram and Scheil-Gulliver CALPHAD simulations address phase formation during solidification, the CALPHAD approach provides more detailed phase fraction evolution and accounts for multicomponent diffusion and intermetallic phases. To compare with the Schaeffler-DeLong diagram predictions, a Scheil-Gulliver simulation was performed, since both approaches aim to represent solidification under non-equilibrium welding conditions. While the Schaeffler–DeLong diagram indicated a fully austenitic microstructure, the Scheil-Gulliver simulation revealed minor delta ferrite and sigma phase, consistent with the SEM observations. This comparison illustrates the advantage of CALPHAD-based Scheil-Gulliver modeling in capturing additional phase equilibria not represented in traditional diagrams. This difference arises because the CALPHAD-based Scheil-Gulliver approach encompasses multicomponent phase equilibria beyond the austenite–ferrite–martensite fields typically depicted in conventional diagrams. Unlike traditional Schaeffler-DeLong diagrams, CALPHAD modeling accounts for multicomponent diffusion and non-equilibrium phase formation, enabling more accurate predictions under rapid cooling conditions representative of welding. This allowed the identification of σ and M23C6 precipitates not foreseen by conventional diagrams.

Under equilibrium conditions, the solidification path of AISI 316 L is characterized by a more stable and narrower solidification range compared to the Scheil-Gulliver model. The simulation illustrates the sequential formation of phases, starting with the liquid phase at high temperatures and proceeding to the precipitation of CR_3SI, G-phase, M_6C carbides, MSI silicides, and SIC. Upon further cooling, the primary FCC austenite phase (FCC_A1) emerges, coexisting with the previously formed secondary phases, and remains stable down to lower temperatures. This pathway reflects minimal microsegregation due to complete diffusion in both solid and liquid phases, leading to a more uniform composition and fewer abrupt phase changes. In Fig. 8 (equilibrium version), these results would be represented by smoother phase boundaries and more gradual phase transitions.

CALPHAD simulations, complemented by scanning electron microscopy (SEM) observations of the fusion zone (FZ) and heat-affected zone (HAZ), revealed the formation of delta ferritic phases alongside secondary phases (refer to Figs. 9 and 11 for detailed micrographs). These microstructural characteristics substantiate the predicted phase evolution as delineated by the thermodynamic simulations, reinforcing the validity of the computational predictions. While the Schaeffler-DeLong diagram predicted a fully austenitic structure, the CALPHAD results and experimental evidence indicate the formation of delta ferrite (δ) and sigma phase (σ) under the non-equilibrium thermal conditions typical of welding. This comparison underscores a divergence between traditional equilibrium-based predictions and more advanced computational

Table 5
Chromium and nickel equivalents for typical AISI 316 L composition values.

Ni (%)	N (%)	Mn (%)	C (%)	$Ni_{(eq)}$	Mo (%)	Si (%)	Nb (%)	Cr (%)	$Cr_{(eq)}$
10.10	0.10	1.20	0.03	14.60	2.00	0.40	0.00	16.80	19.40

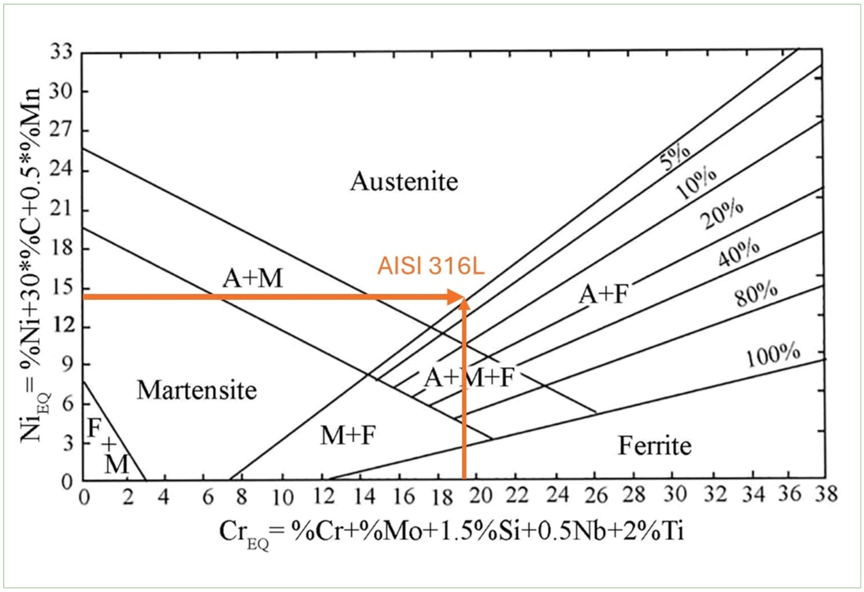

Fig. 6. Schaeffler-Delong Diagram based on estimated Creq and Nieq values for AISI 316 L base metal.

approaches. Although the CALPHAD method predicted minimal influence of niobium on the precipitation of primary chromium carbides, this outcome is attributed to the limited thickness of the electroplated nickel-niobium layer. Fig. 9(A) supports this interpretation by confirming the absence of Nb-rich precipitates such as NbC. Fig. 9(A) shows the sigma phase (σ-phase) found in the heat-affected zone (HAZ) of the welded sample. No sigma phase was detected in the fusion zone (FZ). Although niobium is a potent carbide-former, its effect was limited by the thin coating (~3 μm) and the short duration of the welding thermal cycle. No Nb-rich phases, such as NbC, were detected in the EDS analysis, corroborating the limited Nb diffusion into the weld pool. As niobium diffusion was negligible under the applied thermal cycle, its influence on carbide precipitation was not considered in the CALPHAD input, consistent with the absence of Nb-rich phases in SEM/EDS.

Scheil-Gulliver simulation results indicate a primary ferritic solidification mode, consistent with the Schaeffler-DeLong diagram estimated for the base metal. However, the CALPHAD results predict the presence of a minor sigma phase, which was confirmed by SEM-EDS analysis (Fig. 9).

Although the detailed TC-PRISMA kinetics are not shown, the simulations predicted $M_{23}C_6$ nucleation at ~800 °C, consistent with minor carbide formation observed in the HAZ. These findings underscore the importance of thermal cycle control in welding processes and verify the reliability of CALPHAD simulations as a predictive tool for metallurgical phase stability. The ability to anticipate deleterious phase formation demonstrates the reliability of this valuable input for alloy design, heat-treatment planning, and corrosion-resistance optimization.

3.2. *Microstructural characterization*

Fig. 10 shows scanning electron microscopy (SEM) images in back-scattered electron (BSE) mode with EDS chemical compositions of the AISI 316 L substrate in Fig. 10(A) and the electrodeposited Ni–Watts coating with Nb microparticles on AISI 316 L in Fig. 10(B), taken before the laser welding process. Fig. 10(A) presents austenitic grains containing some thermal twins, with EDS analysis indicating the following composition in Table 6: Fe (58 ± 2 wt%), Cr (18 ± 3 wt%), Ni (8.5 ± 0.6 wt%), and Mo (2 ± 1 wt%). Fig. 10(B) shows the electroplated Ni–Watts grains, with EDS revealing Ni (63 ± 5 wt%), Fe (12 ± 3 wt%), Cr (3 ± 1 wt%), Zn (2 ± 1 wt%), Mo (0.6 ± 0.2 wt%), and Nb only in trace amounts (0.1 ± 0.3 wt%), despite its intentional addition to the plating bath.

Optical and scanning electron microscopy (SEM) micrographs reveal a dendritic solidification morphology in the fusion zone (FZ). Partially recrystallized grains are present in the heat-affected zone (HAZ), as shown in Fig. 11. Fig. 11(a) displays the surface zones after welding, including the HAZ, FZ, and the base metal. This is observed using SEM with secondary electron imaging. In Fig. 11(b), optical microscopy shows that the base metal (BM) microstructure contains α-ferrite grains, dislocation bands, and deformation twins. The base metal primarily exhibits equiaxed α-ferrite grains. The presence of dislocation bands indicates prior plastic deformation.

Deformation twins can form in α-ferrite under high stress or localized strain conditions. However, they are uncommon in body-centered cubic (bcc) structures. Therefore, the twins observed in Fig. 11(b) may also be associated with small amounts of retained austenite. Retained austenite, with its face-centered cubic (fcc) crystal structure, is more likely to twin. This suggests that twinning may result from both α-ferrite and any retained γ-phase. These features contribute to grain subdivision, microstructural refinement, and restricted dislocation movement during deformation.

Ferritoscopy tests and SEM/EDS images confirm that δ-ferrite forms along the edges between dendrites, consistent with CALPHAD predictions of its short-term stability during solidification.

Fig. 11(c) highlights the heat-affected zone (HAZ) and the fusion zone (FZ). The fusion zone consists mainly of an austenitic matrix with a significant amount of delta (δ) ferrite. Sigma (σ) phase precipitates appear in the HAZ, as shown in Fig. 10(d), and display morphologies like those previously reported [95]. Fig. 11(e) provides a detailed analysis of the fusion zone, identifying three δ-ferrite morphologies: skeletal, vermicular, and isolated island ferrite. Each morphology reflects specific solidification conditions. These results are consistent with Scheil–Gulliver CALPHAD predictions, which indicate transient δ-ferrite formation during early solidification, followed by partial δ-to-γ transformation.

In Fig. 11(e), skeletal ferrite is shown as elongated, interconnected networks in the interdendritic regions, indicating rapid solidification with minimal solute back-diffusion. Vermicular ferrite, characterized by worm-like, irregular shapes, appears in areas experiencing moderate constitutional supercooling. Isolated island ferrite is observed as small, discrete, globular pockets surrounded by austenite within Fig. 11(e), typically formed during the final stages of the δ-to-γ transformation.

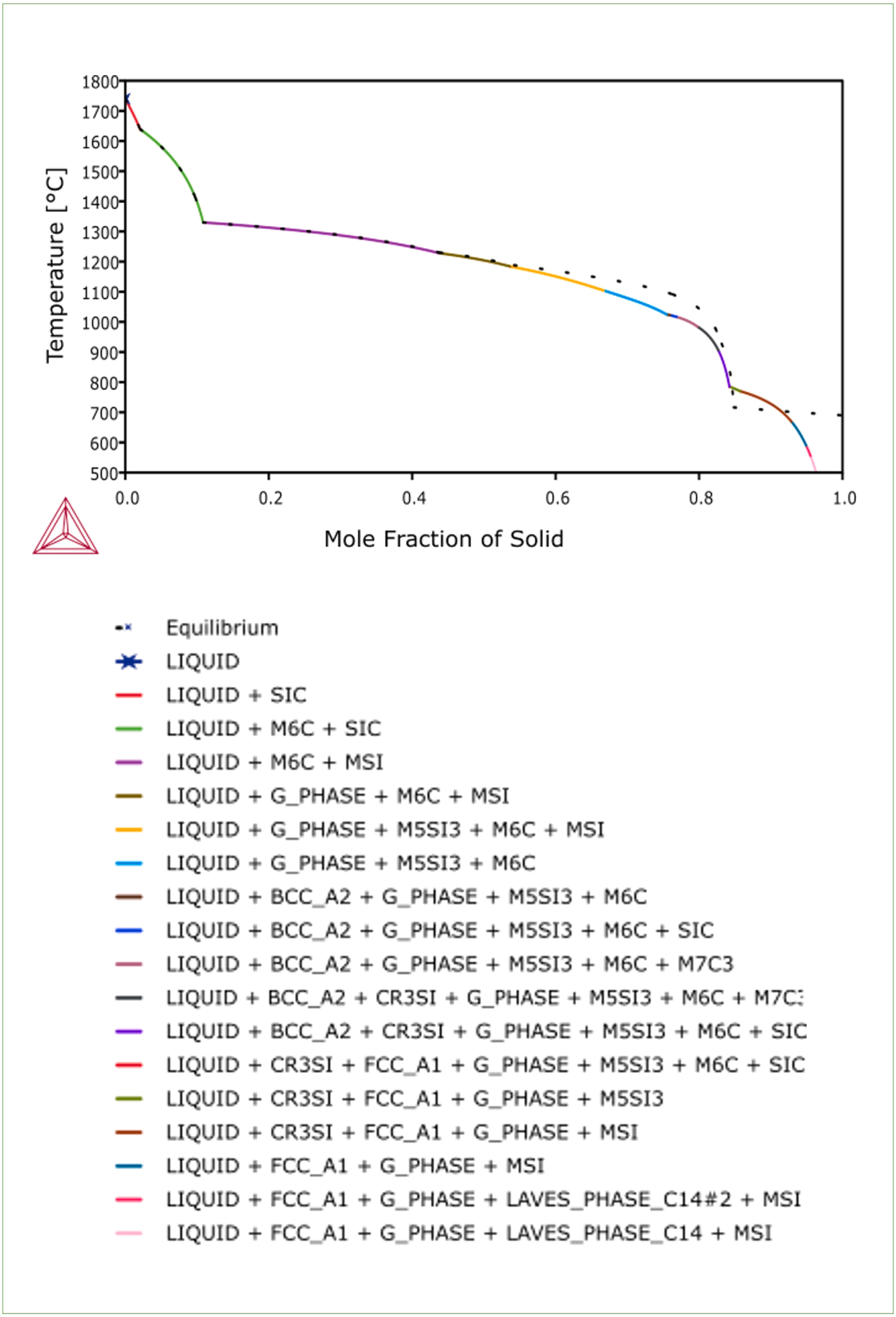

Fig. 7. Solidification Path of AISI 316 L under Scheil-Gulliver Conditions.

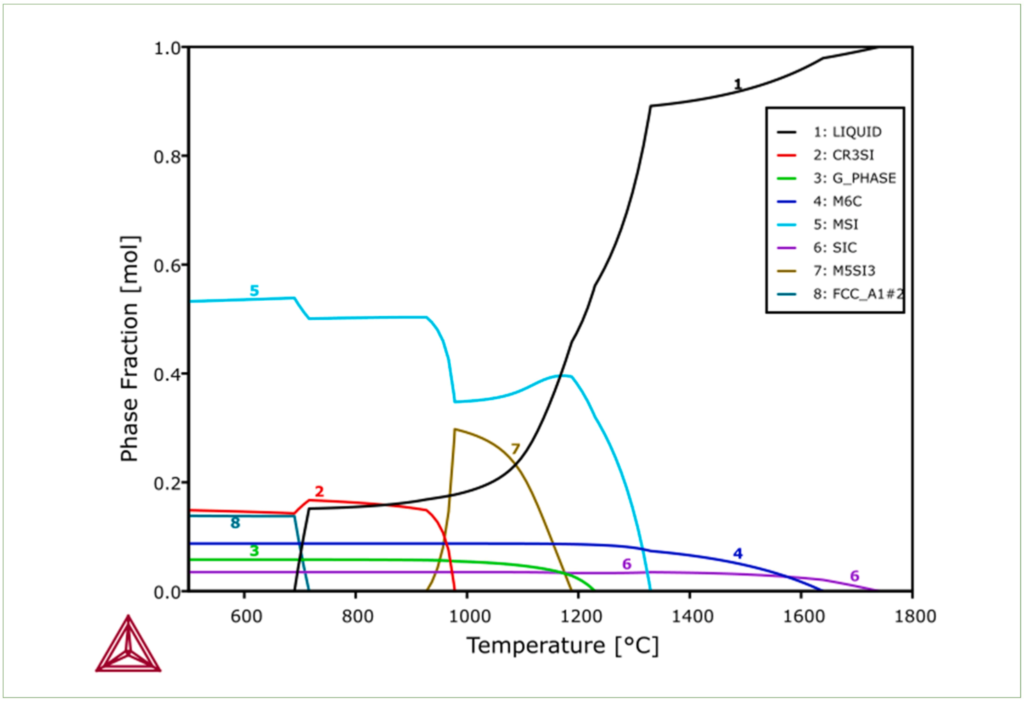

Fig. 8. Solidification Path of AISI 316 L under Equilibrium Conditions.

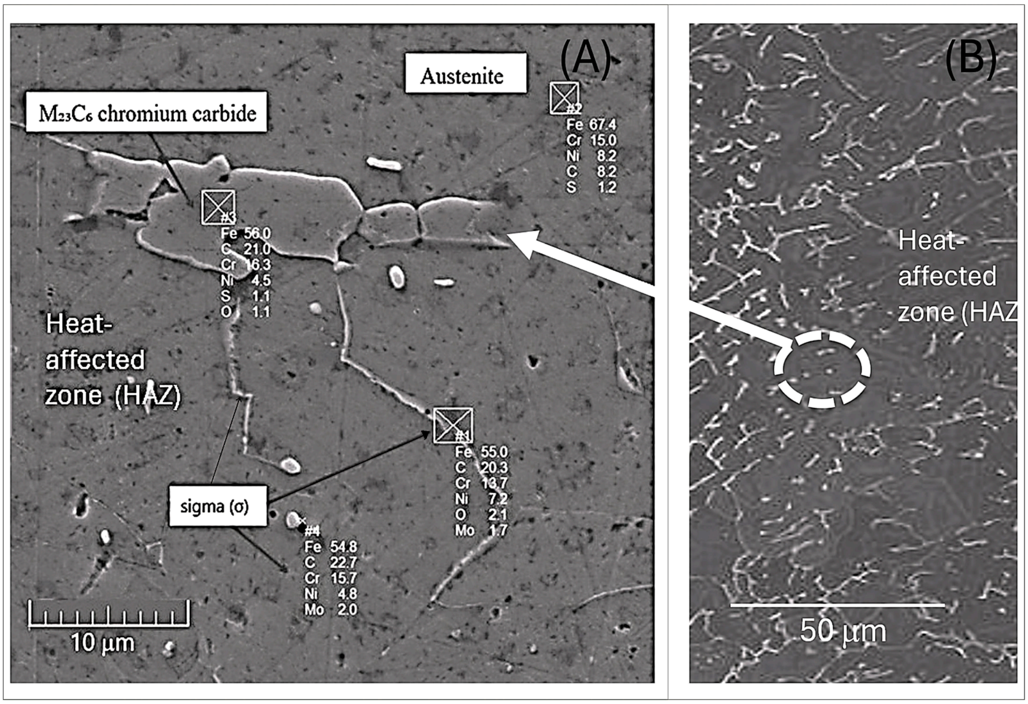

Fig. 9. EDS and SEM micrographs of AISI 316 L stainless steel: (A) EDS spectrum indicating M23C6 and sigma (σ) phase in welded AISI 316 L, (B) heat-affected zone (HAZ, SEM, sigma phase highlighted by arrows).

The ferrite shapes observed in the tests, especially the island and skeletal types, are well matched to CALPHAD Scheil–Gulliver model predictions. These models show that δ-ferrite forms for a short time during early solidification, then partially changes to γ-austenite when cooling is not balanced.

The residual δ-ferrite fractions observed microscopically correspond to small amounts predicted to persist at room temperature. This confirms the agreement between thermodynamic modeling and experimental microstructural evolution. No niobium-rich (Nb-rich) precipitates were detected experimentally, which indicates limited diffusion from the electroplated nickel-niobium (Ni–Nb) layer. It is still important to consider potential microstructural effects if Nb diffusion were more significant. In such cases, predictions from CALPHAD and DICTRA suggest that Nb would stabilize NbC carbides at grain boundaries during cooling. This stabilization could alter chromium activity locally and delay σ-phase nucleation. Enhanced Nb mobility could also

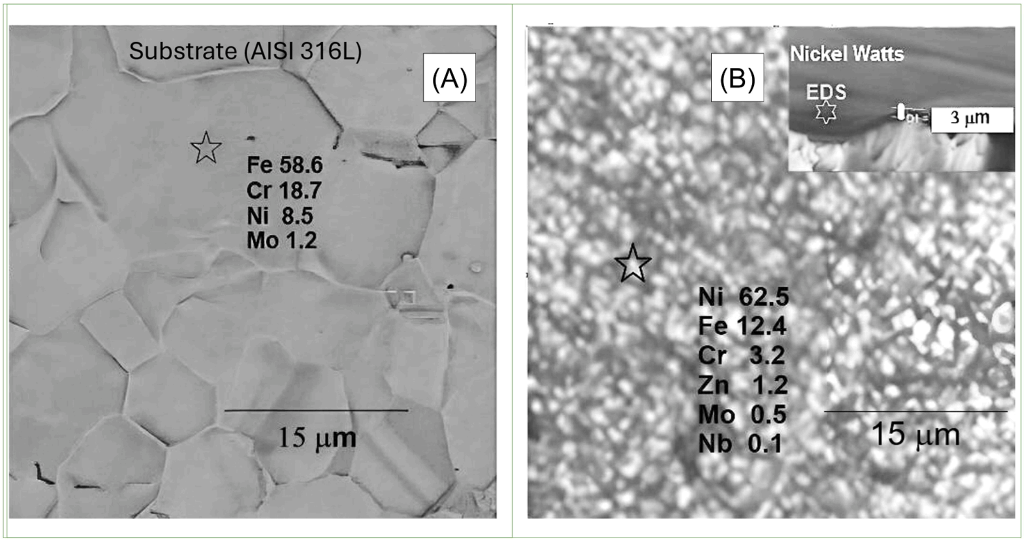

Fig. 10. EDS analysis of the AISI 316 L: (A) substrate; (B) Ni–Watts coating with Nb microparticles, before the laser welding process.

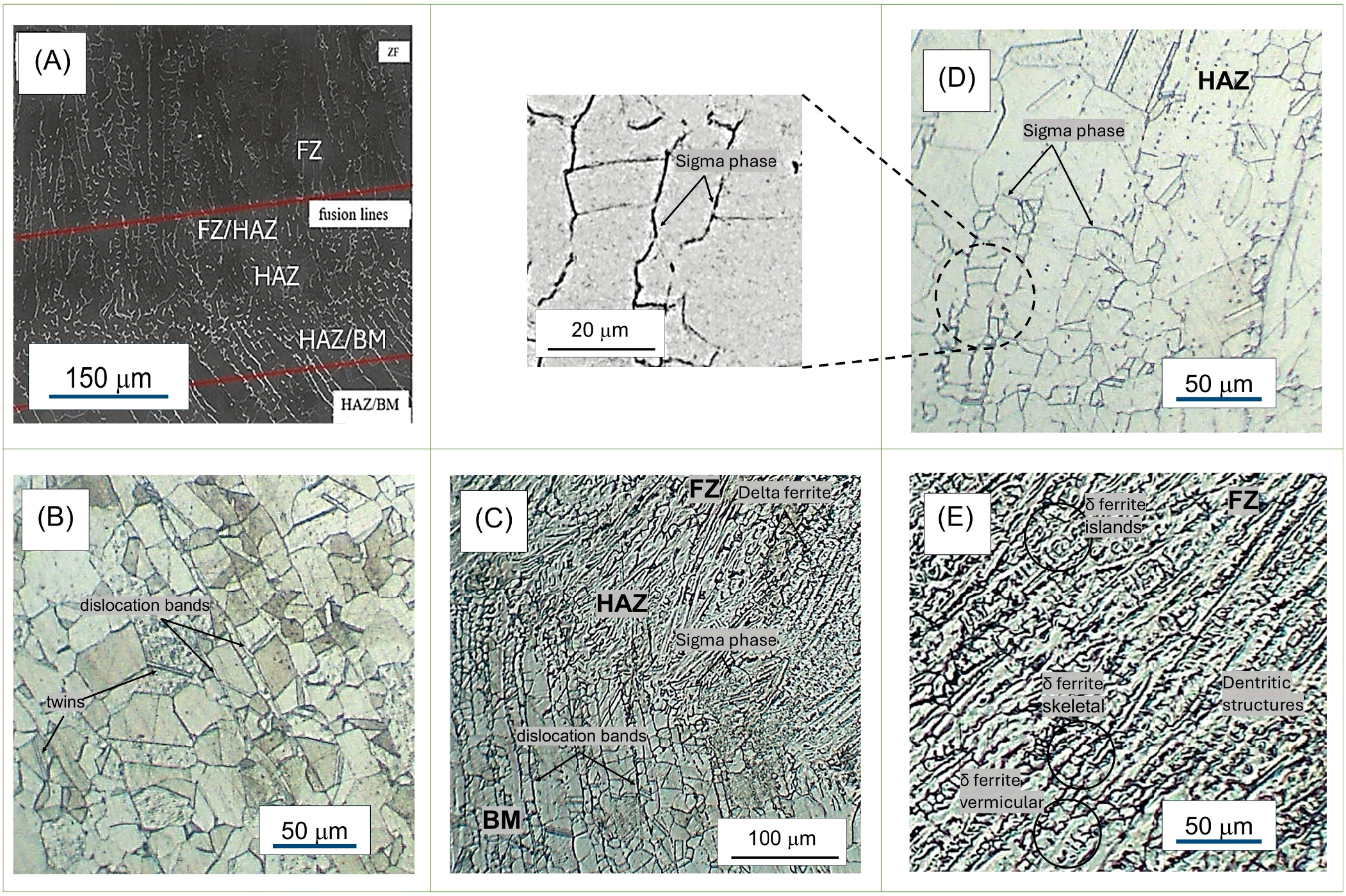

Fig. 11. SEM and optical micrographs of AISI 316 L stainless steel: (A) weld region (SEM); (B) base metal (BM, optical); (C) weld region (optical, delta ferrite and sigma phase highlighted by arrows); (D) heat-affected zone (HAZ, optical); (E) fusion zone (FZ, optical).

affect the δ-to-γ transformation pathway by increasing the thermodynamic driving force for carbide formation. These effects were not observed in the current study due to the thin coating and limited diffusion distances. Nonetheless, they underscore the importance of future DICTRA-based diffusion modeling to quantify Nb mobility across varying coating thicknesses or thermal cycles.

The slight excess of δ-ferrite measured experimentally in the FZ may explain the modest reduction in ductility and the increased corrosion susceptibility observed in subsequent tests. According to the CALPHAD predictions, δ-ferrite stabilizes Cr-rich regions that locally reduce the pitting potential, thus linking phase stability to both mechanical and electrochemical performance.

Table 6
Elemental composition from SEM-EDS analysis (wt%).

Surface	Fe	Cr	Ni	Mo	Zn	Nb
AISI 316 L	58 ± 2	18 ± 3	8.5 ± 0.6	2 ± 1	-	-
Ni–Watts with niobium particles	12 ± 3	3 ± 1	63 ± 5	0.6 ± 0.2	2 ± 1	0.1 ± 0.3

3.3. *Ferritoscopy*

Volumetric ferrite quantification by ferritoscopy, as shown in Fig. 12, revealed a progressive increase in ferromagnetic phase content from the base metal (BM, 0.5 % Fe) to the heat-affected zone (HAZ, 3.3 % Fe), reaching its highest value in the fusion zone (FZ, 6.7 % Fe). This trend reflects the thermal gradient imposed during welding, which favors the retention of delta ferrite because it is stable at high cooling rates.

3.4. *Tensile test results*

The tensile curves (Fig. 13) show that the welded joints exhibit an average ultimate tensile strength (UTS) of 627 ± 27 MPa, whereas the base metal reaches 635 ± 5 MPa. Yield strengths are 367 ± 11 MPa for the welded joints and 355 ± 5 MPa for the BM. Results represent the average of three tests per region (BM, HAZ, and FZ). The slight decrease in UTS and similar YS indicates limited degradation of mechanical integrity, corroborating the microstructural uniformity observed in CALPHAD and microscopy results. The CALPHAD predicts only minor δ-ferrite retention and negligible σ-phase formation, both of which are known to preserve ductility in austenitic stainless steels under non-equilibrium solidification.

Tensile testing indicated that welded joints exhibit slightly lower ultimate tensile strength than the base metal. The engineering stress-strain curves demonstrated that although the ductility was preserved, the presence of intermetallic phases and residual stresses in the FZ contributed to early failure. These results highlight the microstructural sensitivity of AISI 316 L to high thermal input and confirm literature findings on the thermal degradation of mechanical performance post-welding [4].

This observation is consistent with CALPHAD predictions, which indicate negligible σ-phase formation and limited δ-ferrite retention—conditions that maintain the ductility of austenitic stainless steels during rapid solidification.

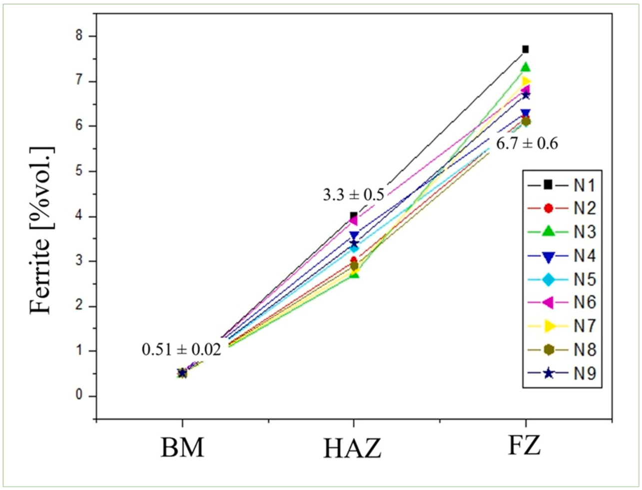

Fig. 12. Volumetric percentage of ferrite in the BM, HAZ, and FZ regions. N1–N9 correspond to the nine tensile specimens: N1–N3 (BM), N4–N6 (HAZ), N7–N9 (FZ).

3.5. *Vickers microhardness*

Table 7 presents the Vickers microhardness results across the weld regions. In the fusion zone (FZ), the microhardness was 231 ± 7 HV. This increase in hardness in the FZ may be attributed to the formation of delta ferrite and possible microsegregation during rapid solidification. The results are consistent with similar GTAW studies, which reported localized hardening due to thermal cycling [96,97].

In the heat-affected zone (HAZ), the microhardness was lower than that of the FZ but higher than that of the base metal (BM), averaging 188 ± 6 HV. The base metal exhibited the lowest average microhardness, at 174 ± 1 HV.

3.6. *Potentiodynamic polarization*

Potentiodynamic polarization tests showed only slight differences in Ecorr and Epit between the base metal (BM) and the welded samples, as illustrated in Fig. 14 and detailed in Table 8. Preservation of passive film integrity across all zones indicates that welding did not significantly compromise corrosion resistance. However, SEM analysis after polarization revealed pitting localized near grain boundaries, due to chromium depletion or phase segregation.

The occurrence of pitting corrosion in AISI 316 L stainless steel, exposed to a 3.5 wt% NaCl saline medium for 3 h and 20 min, as evidenced in Fig. 15 after the polarization tests. The surface examination revealed discrete pitting sites mainly concentrated along interdendritic regions in the FZ. No significant pitting was observed in the BM or HAZ, indicating that corrosion activity was localized mainly within the FZ. No post-weld heat treatment was applied after GTAW, ensuring that the electrochemical results represent the as-welded condition. Pitting was exclusively observed in the fusion zone, while both the HAZ and base metal surfaces remained passive throughout the test duration. This behaviour confirms that corrosion activity is confined to regions predicted by CALPHAD to contain transient δ-ferrite and chromium-depleted boundaries.

Table 8 presents the pitting potential (E_pit) and corrosion potential (E_corr) values derived from datasets generated by the PalmSens software. The samples with a weld bead exhibited an average E_pit of 0.24 ± 0.01 V. In contrast, the base metal (BM) samples recorded an average E_pit of 0.29 ± 0.01 V. Similarly, the welded samples showed an average E_corr of 0.02 ± 0.01 V, compared with 0.05 ± 0.01 V for the BM samples.

These results indicate that welding did not significantly degrade the material's corrosion resistance, as the pitting potential of the welded specimens remained close to that of the base metal. Although the passivating current was not directly measured, the slight reductions in both E_pit and E_corr for the coated-welded samples suggest that the Ni–Nb coating maintained the integrity of the passive film during thermal cycling.

Future work will include electrochemical impedance spectroscopy (EIS) to confirm the passive film kinetics and assess long-term stability. Variations in passivating current can provide insights into changes in the defect structure of Cr_2O_3 films arising from Ni and Nb incorporation during electroplating. Although not measured here, such data could offer a deeper understanding of passive film stability on Nb- and Ni-enriched surfaces.

3.7. *Fractographic analysis*

SEM fractography in Fig. 16 shows ductile fracture in all regions. The fracture surfaces contain numerous dimples. The weld and HAZ undergo microstructural changes. Still, the material retains plastic deformation before a rupture. The weld zone shows dimples of different sizes. This suggests heterogeneous deformation due to phase contrast between austenite and delta ferrite.

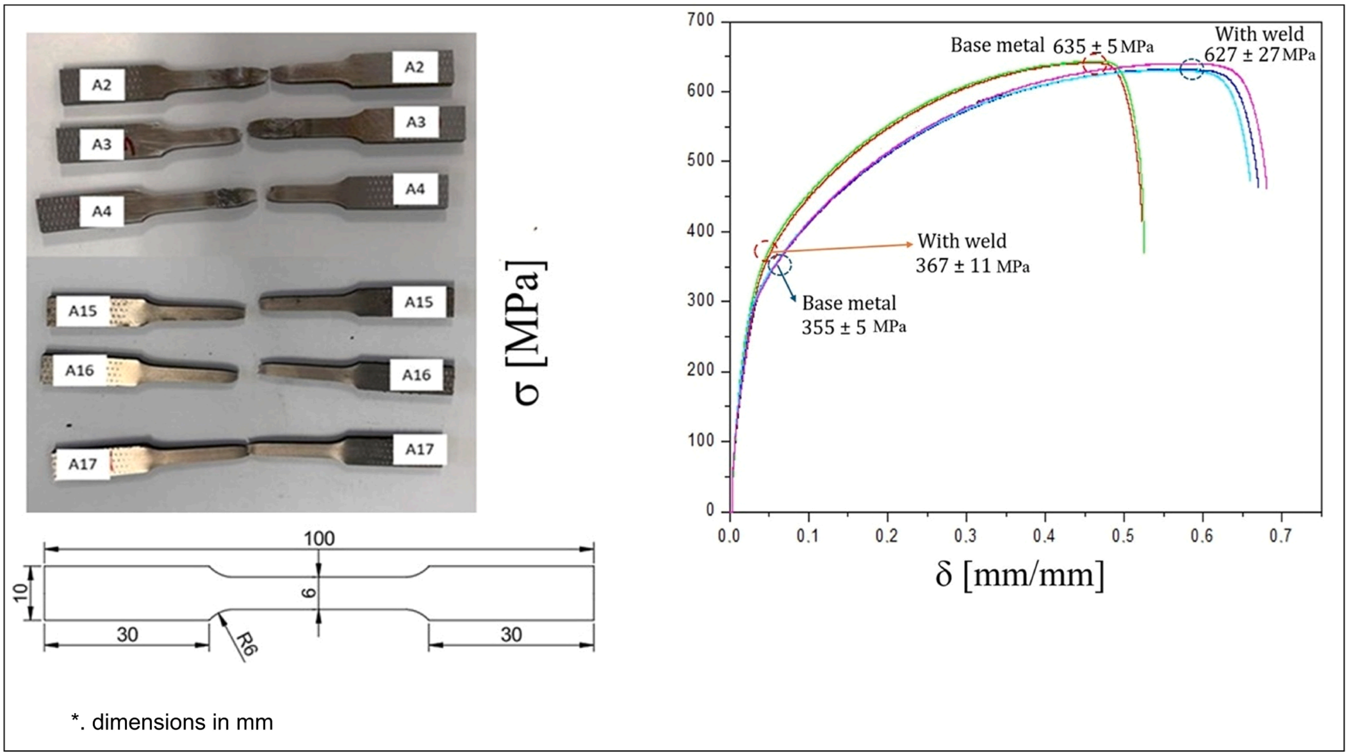

Fig. 13. Engineering stress–strain behaviour of the base metal (BM) and welded regions (FZ and HAZ). Tensile specimens A2–A3 (BM), A4 (HAZ), and A15–A17 (FZ) are shown. Consistent colour and line styling are employed to allow direct comparison of yield and ultimate tensile strength across all sampled regions.

Table 7
Vickers microhardness values across weld regions.

Weld Region	Vickers Hardness (HV ± SD)
Fusion Zone (FZ)	231 ± 7
Heat-Affected Zone (HAZ)	188 ± 6
Base Metal (BM)	174 ± 1

3.8. Limitations and outlook

Niobium diffusion was negligible under the current welding conditions due to the thin coating (approximately 2–3 µm) and the short thermal cycle. However, possible phase-transformation pathways arising from increased niobium mobility are under consideration. CALPHAD–DICTRA predictions indicate that extended diffusion may stabilize NbC carbides, change local chromium activity, and delay sigma-phase nucleation. Future research will address these effects by studying niobium transport kinetics and assessing the influence of prolonged thermal exposure on microstructural stability and corrosion resistance.

4. Conclusions

The present work integrated CALPHAD-based thermodynamic and kinetic simulations with experimental validation to evaluate the phase evolution in GTAW-welded AISI 316 L stainless steel coated with a Ni–Nb layer. The CALPHAD approach accurately predicted the solidification sequence and transformation behavior of the alloy, with δ-ferrite appearing transiently in the fusion zone and being replaced by γ-austenite during cooling.

The σ-phase and $M_{23}C_6$ carbides were predicted only in trace amounts at low temperatures, which was consistent with the microstructural features observed by SEM/EDS. Ferritoscopy measurements confirmed a small but measurable δ-ferrite content, in good agreement with the non-equilibrium Scheil–Gulliver calculations.

Tensile and microhardness results indicated minimal degradation in mechanical properties after welding, confirming that the coating and process parameters maintained the material's structural integrity.

Electrochemical tests revealed slightly higher corrosion currents in the welded samples, but no significant loss of passivity was observed. The Ni–Nb coating contributed to improved pitting resistance compared with uncoated 316 L.

Experimental analyses confirmed the presence of these phases, particularly the precipitation of intermetallic compounds along grain boundaries in the heat-affected zone. The fusion zone exhibited the highest ferrite content and corresponding increases in microhardness, consistent with the thermal gradients imposed by the welding process. Despite the incorporation of niobium by electrodeposition, no Nb-rich precipitates were identified, attributed to the coating's thin thickness and restricted diffusion during welding.

The combined use of CALPHAD modelling and experimental verification has proven to be a robust approach for correlating predicted phase stability with the actual microstructures of welded joints, providing valuable insights into the design of surface-engineered stainless-steel systems with enhanced mechanical and corrosion performance. While the nickel-niobium coating had a minimal impact on phase formation under the studied conditions, the integrated modeling approach provides strategic insights for developing advanced stainless steel components with enhanced structural and chemical performance.

Future studies will extend CALPHAD simulations to account for Nb diffusion profiles during prolonged thermal cycles and evaluate their effect on long-term phase stability. Furthermore, integrating CALPHAD-based modelling with real-time thermal cycle data could enable predictive control of weld metallurgy in automated manufacturing. This direction, combined with extended DICTRA–PRISMA coupling, represents a pathway for developing innovative, corrosion-resistant stainless-steel systems tailored for next-generation energy, industrial welding process design, and biomedical applications.

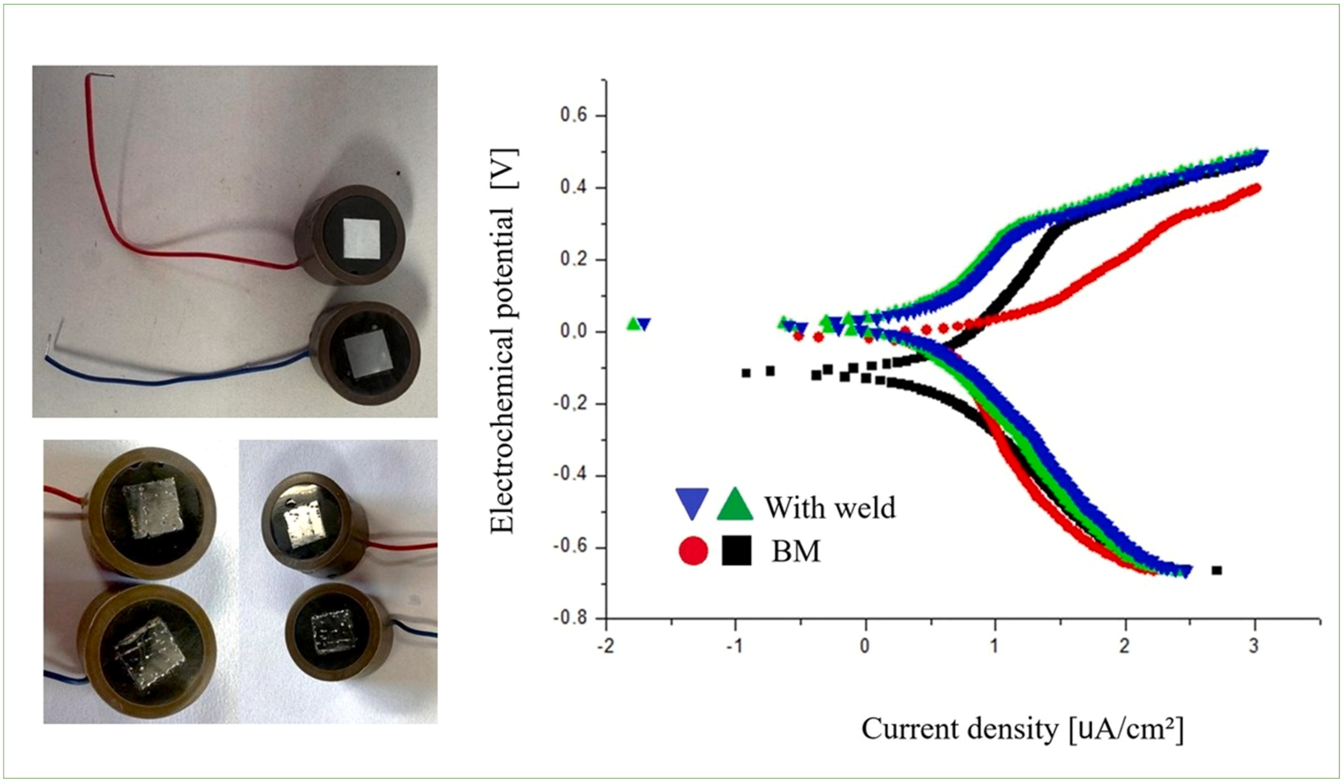

Fig. 14. Potentiodynamic polarization curves of AISI 316 L austenitic stainless steel (three-electrode cell, 3.5 wt% NaCl, 25 °C, 0.167 mV s^{-1}). The welded sample shows a slightly more negative $E_{(corr)}$ and higher $I_{(corr)}$ than the BM, suggesting minor localized depassivation near the FZ.

Table 8
Electrochemical parameters obtained from potentiodynamic polarization tests in a three-electrode cell, 3.5 wt% NaCl, 25 °C, 0.167 mV·s^{-1} .

Sample	$E_{(corr)}$ (V) Mean ± SD	$E_{(pit)}$ (V) Mean ± SD
Base Metal (BM)	0.05 ± 0.01	0.29 ± 0.01
Welded Sample	0.02 ± 0.01	0.24 ± 0.01

Ethical approval

In this work, experiments involving human tissue were not conducted, and approval from the institutional review board or an equivalent ethics committee is not required.

Funding

The authors do not have any research funding to support this publication.

CRediT authorship contribution statement

de Brito Tarcísio Golçalves: Writing – review & editing. **Haroldo Lhou Hasegawa:** Writing – review & editing. **Rogério Fernandes Brito:** Writing – review & editing. **Renata Neves Penha:** Writing – review & editing. **Ricardo Luiz Perez Teixeira:** Writing – review & editing, Writing – original draft. **Eduardo Miguel da Silva:** Writing – review & editing. **José Carlos de Lacerda:** Writing – review & editing. **Vilas Boas Sebastiao Bruno:** Writing – review & editing. **Rafael Nascimento:** Writing – original draft. **Allexia Izabella Pinheiro Damasceno:** Writing – original draft.

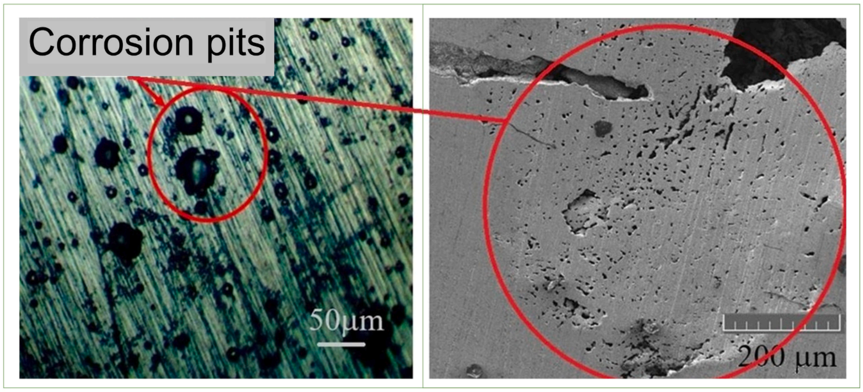

Fig. 15. Surface morphology after polarization testing, showing isolated corrosion pits mainly along interdendritic zones in the FZ, consistent with chromium depletion predicted by CALPHAD.

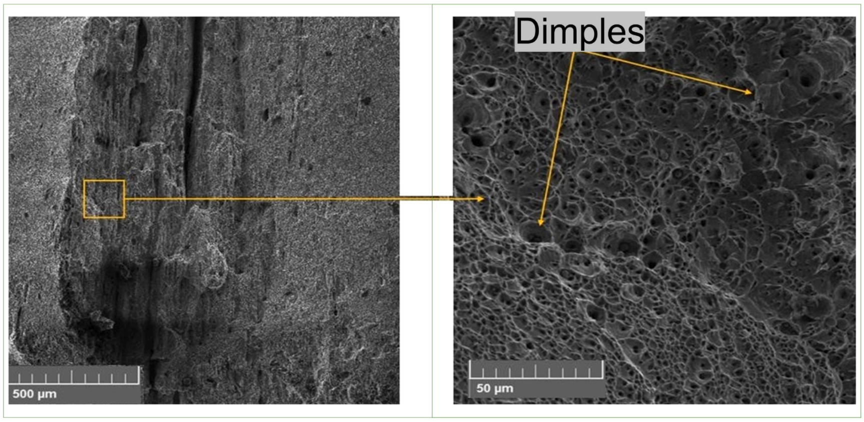

Fig. 16. Fractographic SEM images of fractured specimens after tensile testing, revealing ductile failure with equiaxed dimples and negligible cleavage, confirm that the welding and coating procedures preserved the ductility of the alloy.

Declaration of Generative AI and AI-assisted technologies in the writing process

The authors declare that no generative AI or AI-assisted technologies were used in the writing of this manuscript.

Declaration of Competing Interest

The authors declare that they have no known competing financial interests or personal relationships that could have appeared to influence the work reported in this paper.

Acknowledgments

The authors warmly thank the Institute of Integrated Engineering and Limav (Interdisciplinary Laboratory for Advanced Materials) for invaluable laboratory support and PRPPG (professional master's degree in materials engineering) for administrative assistance at the Federal University of Itajubá.

Author contributions

RLP Teixeira, AIP Damasceno, SB Vilas Boas, and JC de Lacerda contributed to the original manuscript. RLP Teixeira, SB Vilas Boas, JC de Lacerda, RN Penha, RF Brito, TG de Brito, HL Hasegawa, and EM da Silva were responsible for review and editing.

Appendix A. Supporting information

Supplementary data associated with this article can be found in the online version at doi:10.1016/j.mtcomm.2025.114537.

Data availability

The phase simulation prompt is provided in the supplementary material.

References

[1] A.V.M. Marques, K.M.D. Carmo, W.C. Lage, R.L.P. Teixeira, J.C.D. Lacerda, C.H.S. B. Teixeira, R. Shitsuka, Avaliação do efeito de deformação plástica na dureza, microestrutura e propriedades magnéticas de um aço inoxidável AISI 316L, Mat. éria (Rio J. 25 (2020) e-12611, https://doi.org/10.1590/s1517-707620200002.1011.

[2] L.G.F. Silva, R.L.P. Teixeira, G.O. Siqueira, J.C. de Lacerda, Design na Educação para Iniciação Científica em Pesquisa Sobre o Efeito TRIP em Ciência dos Materiais, Br. J. Ed. Tech. Soc. 17 (2024) 1050–1064, https://doi.org/10.14571/brajets.v17.n3.1050-1064.

[3] R.L.P. Teixeira, J.C. De Lacerda, K.C. Florencio, S.N. Da Silva, A.B. Henriques, TRIP effect produced by cold rolling of austenitic stainless steel AISI 316L, J. Mater. Sci. 58 (2023) 3334–3345, https://doi.org/10.1007/s10853-023-08235-7.

[4] E.M. da Silva, R.L.P. Teixeira, S.C. da Costa, E.O. Corrêa, R.B. Ribeiro, Stress-corrosion cracking behavior of AISI-409 Welded with a filler metal flux cored AWS E316LT1-4, Mat. Res. 27 (2024) e20230418, https://doi.org/10.1590/1980-5373-MR-2023-0418.

[5] R.L.P. Teixeira, P.C.D. Silva, Advancing metallic biomaterials for biomedical implants: a comprehensive integrative review, RGSA 18 (2024) e05255, https://doi.org/10.24857/rgsa.v18n5-036.

[6] J.C.D. Lacerda, R.L.P. Teixeira, R.M.R.D. Souza, R.B. Soares, V.D.F.C. Lins, Pitting Corrosion Behavior of UNS S31803 and UNS S32304 Duplex Stainless Steels in 3.5 wt% NaCl Solution, Mat. éria (Rio J. 25 (2020), https://doi.org/10.1590/s1517-707620200002.1022.

[7] K. Hrabovská, O. Životský, P. Váňová, Y. Jirásková, L. Gembalová, O. Hilšer, Microstructure and magnetism of austenitic steels in relation to chemical composition, severe plastic deformation, and solution annealing, Sci. Rep. 15 (2025), https://doi.org/10.1038/s41598-025-86028-5.

[8] H. Granados Becerra, A. Ruiz, V.H. López Morelos, M.A. Espinosa Medina, A. Medina Flores, Microstructural characterization, mechanical, and intergranular corrosion of an Inconel 625 - AL6XN super austenitic stainless steel welded joint, MRS Adv. 9 (2024) 1923–1930, https://doi.org/10.1557/s43580-024-00994-y.

[9] L. Chen, Y. Wang, Y. Li, Z. Zhang, Z. Xue, X. Ban, C. Hu, H. Li, J. Tian, W. Mu, K. Yang, C. Chen, Effect of Nickel content and cooling rate on the microstructure of as-cast 316 stainless steels, Crystals 15 (2025) 168, https://doi.org/10.3390/cryst15020168.

[10] P.R. John Raj Kumar, A. Baskaran, D. Thirumalaikumarasamy, T. Sonar, M. Ivanov, R. Pavendhan, Microstructure and mechanical properties of double pulse TIG welded super austenitic stainless steel butt joints, Mater. Test. 66 (2024) 1379–1387, https://doi.org/10.1515/mt-2024-0081.

[11] L. Quackatz, E.M. Westin, A. Griesche, A. Kromm, T. Kannengiesser, K. Treutler, V. Wesling, S. Wessman, Assessing ferrite content in duplex stainless weld metal: WRC '92 predictions vs. practical measurements, Weld. World 69 (2025) 31–45, https://doi.org/10.1007/s40194-024-01878-3.

[12] P. Noga, T. Skrzekut, M. Wędrychowicz, M.St Węglowski, M. Wiewióra, The influence of various welding methods on the microstructure and mechanical properties of 316Ti steel, Materials 17 (2024) 1681, https://doi.org/10.3390/ma17071681.

[13] L.H.R. Apolinário, H.R. Araújo, I.J. Marques, E.A. Torres, T.F.A. Santos, Microstructural evaluation of 316L composite coatings reinforced with niobium carbide particle produced by laser cladding, Mater. Werkst. 56 (2025) 419–437, https://doi.org/10.1002/mawe.202400214.

[14] S.S. Jogdand, A. Niklas, D. Linder, F. Santos, C. Hulme, B. Glaser, A modified AISI 310 steel family: Microstructure engineering for high-temperature load-bearing applications, Mater. High. Temp. 42 (2025) 102–121, https://doi.org/10.1080/09603409.2025.2469963.

[15] A. Xie, S. Chen, S. Chen, H. Jiang, L. Rong, Austenite decomposition behavior adjacent to δ-ferrite in a Si-modified Fe-Cr-Ni austenitic stainless steel during thermal aging at 550 °C, Acta Mater. 272 (2024) 119948, https://doi.org/10.1016/j.actamat.2024.119948.

[16] A01.17 Committee (2022) ASTM A240/A240M-22a, Specification for Chromium and Chromium-Nickel Stainless Steel Plate, Sheet, and Strip for Pressure Vessels and for General Applications. 〈https://store.astm.org/a0240_a0240m-22a.html〉.

[17] A. Sarkar, Influence of welding heat input and post-weld heat treatment on mechanical and microstructural properties of modified 9Cr-1Mo (P91) steel in submerged arc welding, Weld. Int. 39 (2025) 309–321, https://doi.org/10.1080/09507116.2025.2461638.

[18] A.R. Pimenta, I.P. Baptista, I.M.D.S. Breves, J.M. Pardal, S.S.M. Tavares, Effects of post-weld heat treatments in microstructure, mechanical properties, and corrosion resistance of simulated heat-affected zone of supermartensitic steel UNS S41426,

Int. J. Adv. Manuf. Technol. 132 (2024) 1915–1929, https://doi.org/10.1007/s00170-024-13448-4.

[19] M. Mičian, M. Frátrik, M. Brůna, Softening effect in the heat-affected zone of laser-welded joints of high-strength low-alloyed steels, Weld. World 68 (2024) 1497–1514, https://doi.org/10.1007/s40194-024-01730-8.

[20] Z. Wang, X. Wang, C. Shang, Effect of pre-weld heat treatment on the microstructure and properties of coarse-grained heat-affected zone of a wind power steel after simulated welding, Metals 14 (2024) 587, https://doi.org/10.3390/met14050587.

[21] O. Falodun, S. Oke, M. Bodunrin, A comprehensive review of residual stresses in carbon steel welding: formation mechanisms, mitigation strategies, and advanced post-weld heat treatment techniques, Int J. Adv. Manuf. Technol. 136 (2025) 4107–4140, https://doi.org/10.1007/s00170-025-15088-8.

[22] H.B. Zhang, Z.W. Wang, P. Xue, J.H. Li, W.G. Wang, H. Zhang, D.R. Ni, F.C. Liu, B. L. Xiao, Z.Y. Ma, Eliminating heat-affected zone of nuclear heat-resistant steel joint via low-temperature friction stir welding, Mater. Sci. Eng. A 916 (2024) 147340, https://doi.org/10.1016/j.msea.2024.147340.

[23] J. Cao, Z. Liu, M. Zhai, L. Qiao, Z. Lei, M. Wang, R. Li, A review on hydrogen embrittlement of welded joint of low-alloy steel: focusing on welding technologies, J. Iron Steel Res. Int. (2025), https://doi.org/10.1007/s42243-025-01485-6.

[24] R.E. Chauke, C.W. Siyasiya, D. Nyabadza, The role of niobium during heat treatment of high-vanadium high-speed steel rolls for improved mechanical properties, Metallogr. Microstruct. Anal. 13 (2024) 1140–1152, https://doi.org/10.1007/s13632-024-01142-6.

[25] A.V. Benedito, C.A. Benedetty Torres, R.M.D.C. Silva, P.A. Krahl, D.C.T. Cardoso, F. D.A. Silva, C.H. Martins, Effects of niobium addition on the mechanical properties and corrosion resistance of microalloyed steels: a review, Buildings 14 (2024) 1462, https://doi.org/10.3390/buildings14051462.

[26] S. Liu, X.-X. Ye, T. Wu, W. Yin, H. Chen, J. Xu, X. Zhou, Effects of Nb addition on the carbides, grain boundary characteristics and tensile properties of a Ni–26W–6Cr-based superalloy, Mater. Sci. Eng. A 894 (2024) 146176, https://doi.org/10.1016/j.msea.2024.146176.

[27] 316L 1.4404 - Austenitic - Stainless Steel, Aperam (n.d.). ⟨https://www.aperam.com/product/316l-1-4404/⟩ (accessed May 1, 2025).

[28] I. Nunes, R. Teixeira, V. Signoretti, J. Lacerda, Effect of nickel-niobium coating on fatigue resistance of SAE 1020 carbon steel, Int. J. Eng. Res. Technol. 6 (2017) 397–401, https://doi.org/10.17577/IJERTV6IS010279.

[29] H. Aghajani, M.B. Balajaddeh, M. Pouranvari, Transitioning solidification mode via electroplated Ni coatings in martensitic stainless steel resistance spot welds: new insights into fabricating tough microstructure, Sci. Rep. 14 (2024), https://doi.org/10.1038/s41598-024-53897-1.

[30] M.C. Asirvatham, I. Masters, G. West, C. Harris, Influence of nickel-plating on laser weldability of aluminium busbars for lithium-ion battery interconnects, J. Mater. Res. Technol. 36 (2025) 4501–4515, https://doi.org/10.1016/j.jmrt.2025.04.110.

[31] M. Francioso, C. Angeloni, A. Fortunato, E. Liverani, A. Ascari, Experimental investigation on the effect of nickel-plating thickness on continuous-wave laser welding of copper and steel tab joints for battery manufacturing, Lasers Manuf. Mater. Process 11 (2024) 353–370, https://doi.org/10.1007/s40516-024-00246-9.

[32] Y. Fei, X. Wang, H. Yue, H. Zou, Y. Zhao, A. Wu, Debonding mechanisms and prevention of electroformed nickel/copper–zirconium alloy in the thrust chamber under arc welding conditions, J. Mater. Res. Technol. 36 (2025) 4354–4365, https://doi.org/10.1016/j.jmrt.2025.04.159.

[33] H. Qin, H. Bao, C. Zhang, K. Pan, X. Zhao, Influence of nickel plating on the welding metallurgical mechanism, microstructure, and shear performance of C101/80Au20Sn/C101 solder joints, Mater. Charact. 215 (2024) 114166, https://doi.org/10.1016/j.matchar.2024.114166.

[34] N.Y. Elamin, M.R. Elamin, H. Alhussain, R.F.M. Elshaarawy, M.I.A. Habba, R. A. Fouad, Influence of Cu and Ni addition on metallurgical, mechanical, and corrosion behavior of TIG welded Al-Mg-Si alloy, Int. J. Press. Vessels Pip. 216 (2025) 105533, https://doi.org/10.1016/j.ijpvp.2025.105533.

[35] W, T. Ulitzka, L. Dahl, L. Wojarski, H. Ulitzka, M. Koymatli, Application of nickel plating by galvanization on the steel surface of brazed cemented carbide-maraging steel joints, Weld. World 67 (2023) 1313–1324, https://doi.org/10.1007/s40194-022-01461-8.

[36] X. Huang, J. Wang, Y. Wu, Y. Wang, P. Liu, Z. Chen, S. Zheng, A Threshold Cr Domin. Struct. Transit. Stab. Enhanc. Passiv. Films High. Entropy Alloy Crxmnfeconi (2025), https://doi.org/10.2139/ssrn.5081278.

[37] S.B. Inman, M.A. Wischhusen, J. Qi, S.J. Poon, S.R. Agnew, J.R. Scully, Variation of the passive film on compositionally concentrated dual-phase Al0.3Cr0.5Fe2Mn0.25Mo0.15Ni1.5Ti0.3 and implications for corrosion, Met. Mater. Trans. A 55 (2024) 4776–4795, https://doi.org/10.1007/s11661-024-07572-9.

[38] S.-C. Kim, H. Tsuchiya, T. Manaka, T. Hanawa, S. Fujimoto, Electronic structures of passive film formed on Ti and Cr in a phosphate buffer solution of pH 7, J. Electrochem. Soc. 171 (2024) 031506, https://doi.org/10.1149/1945-7111/ad32a4.

[39] E.H. Hwang, J.S. Park, H.G. Seong, S.J. Kim, Analysis on surface film formed on high-strength carbon steels in acidic phosphate solution and its relationship with localized corrosion in a 3.5% NaCl solution, J. Mater. Res. Technol. 8 (2019) 1419–1426, https://doi.org/10.1016/j.jmrt.2018.10.007.

[40] M. Liu, C. Du, Z. Liu, L. Wang, R. Zhong, X. Cheng, J. Ao, T. Duan, Y. Zhu, X. Li, A review on pitting corrosion and environmentally assisted cracking on duplex stainless steel, Microstructures (2023), https://doi.org/10.20517/microstructures.2023.02.

[41] J. Singh, A.S. Shahi, Electrochemical corrosion behavior and microstructural characteristics of electron beam welded UNS S32205 duplex stainless steel, Mater. Corros. 72 (2021) 1350–1369, https://doi.org/10.1002/maco.202012201.

[42] I.M.-B. Omiogbemi, D.S. Yawas, A. Das, M.O. Afolayan, E.T. Dauda, R. Kumar, S. R. Gorja, S.G. Chowdhury, Mechanical properties and corrosion behaviour of duplex stainless steel weldment using novel electrodes, Sci. Rep. 12 (2022), https://doi.org/10.1038/s41598-022-26974-6.

[43] Pycalphad, in: Zentropy (Ed.), Calphad-Based Computational Thermodynamics in Python, 1st ed., Jenny Stanford Publishing, New York, 2024, pp. 373–392, https://doi.org/10.1201/9781003514466-18.

[44] Y. Li, B. Holmedal, B. Liu, H. Li, L. Zhuang, J. Zhang, Q. Du, J. Xie, Towards high-throughput microstructure simulation in compositionally complex alloys via machine learning, Calphad 72 (2021) 102231, https://doi.org/10.1016/j.calphad.2020.102231.

[45] M.A. Chernigin, S.A. Sorokina, R.A. Vorobyev, Study of the microstructure of metastable austenitic chromium manganese steel 14Kh15G9ND by optical and electron microscopy, Zavod. Lab. Diagn. Mater. 89 (2023) 38–44, https://doi.org/10.26896/1028-6861-2023-89-4-38-44.

[46] N. Oliveira Da Vera, I. Holanda Pessoa Pio, F. Da Barbosa Da Luz, A. De Sá Brandim, R. Carvalho Leite, Procedures for preparing metallic specimens for submission to optical microscopy, CONJ 22 (2022) 93–109, https://doi.org/10.53660/CONJ-934-K05.

[47] S. Lu, Z. Zhang, Y. Tang, S. Li, S. Bai, Enhancing phase stability in low-activation TiVTa-based alloys through CALPHAD-guided design, JOM 77 (2025) 1524–1535, https://doi.org/10.1007/s11837-024-07023-1.

[48] C. Zang, X. Zhao, H. Xia, W. Wen, Z. Tan, C. Tan, P.E.J. Rivera-Díaz-del-Castillo, Design method of immiscible dissimilar welding (Mg/Fe) based on CALPHAD and thermodynamic modelling, Mater. Des. 243 (2024) 113050, https://doi.org/10.1016/j.matdes.2024.113050.

[49] S. Gorsse, O. Senkov, About the reliability of CALPHAD predictions in multicomponent systems, Entropy 20 (2018) 899, https://doi.org/10.3390/e20120899.

[50] D.S. Konadu, P.G.H. Pistorius, Investigation of formation of precipitates and solidification temperatures of ferritic stainless steels using differential scanning calorimetry and Thermo-Calc simulation, Sādhanā 46 (2021), https://doi.org/10.1007/s12046-021-01672-7.

[51] C. Quitzke, M. Hauser, L. Krüger, O. Volkova, M. Wendler, Solidification of tungsten inert gas–welded austenitic stainless steel with 0.17 wt% N, Steel Res. Int. (2024), https://doi.org/10.1002/srin.202400244.

[52] S.K. Saha, A. Kumar, Coupled temperature-microstructure model for predicting temperature distribution and phase transformation in steel for arbitrary cooling curves, J. Therm. Sci. Eng. Appl. 13 (2021), https://doi.org/10.1115/1.4048212.

[53] R. Bender, D. Féron, D. Mills, S. Ritter, R. Bäßler, D. Bettge, I. De Graeve, A. Dugstad, S. Grassini, T. Hack, M. Halama, E. Han, T. Harder, G. Hinds, J. Kittel, R. Krieg, C. Leygraf, L. Martinelli, A. Mol, D. Neff, J. Nilsson, I. Odnevall, S. Paterson, S. Paul, T. Prošek, M. Raupach, R.I. Revilla, F. Ropital, H. Schweigart, E. Szala, H. Terryn, J. Tidblad, S. Virtanen, P. Volovitch, D. Watkinson, M. Wilms, G. Winning, M. Zheludkevich, Corrosion challenges towards a sustainable society, Mater. Corros. 73 (2022) 1730–1751, https://doi.org/10.1002/maco.202213140.

[54] Y. Xu, Y. Li, T. Chen, C. Dong, K. Zhang, X. Bao, A short review of medical-grade stainless steel: Corrosion resistance and novel techniques, J. Mater. Res. Technol. 29 (2024) 2788–2798, https://doi.org/10.1016/j.jmrt.2024.01.240.

[55] R. Francis, G. Byrne, Duplex stainless steels—alloys for the 21st century, Metals 11 (2021) 836, https://doi.org/10.3390/met11050836.

[56] Joseph Nnaemeka Chukwunweike, Andrew Nii Anang, Adewale Abayomi Adeniran, Jude Dike, Enhancing manufacturing efficiency and quality through automation and deep learning: addressing redundancy, defects, vibration analysis, and material strength optimization, World J. Adv. Res. Rev. 23 (2024) 1272–1295, https://doi.org/10.30574/wjarr.2024.23.3.2800.

[57] Sustainability in Welding Industries, in: Automation in Welding Industry, 1st ed., Wiley, 2024, pp. 215–228, https://doi.org/10.1002/9781394172948.ch12.

[58] E. Doncheva, N. Avramov, A. Krstevska, M. Petreski, J. Djokikj, M. Djidrov, Sustainability and environmental life cycle analysis of welding processes, IJSI (2024), https://doi.org/10.1108/ijsi-02-2024-0024.

[59] I. Zakharova, Welding processes in the restoration of industrial and energy facilities, Teh. ìka ta Energ. 15 (2024) 56–64, https://doi.org/10.31548/machinery/1.2024.56.

[60] A. Kaimkuriya, B. Sethuraman, M. Gupta, Effect of Physical Parameters on Fatigue Life of Materials and Alloys: A Critical Review, Technologies 12 (2024) 100, https://doi.org/10.3390/technologies12070100.

[61] K. Stankiewicz, A. Lipkowski, P. Kowalczyk, M. Giżyński, B. Waśniewski, Resistance Welding of Thermoplastic Composites, Including Welding to Thermosets and Metals: A Review, Materials 17 (2024) 4797, https://doi.org/10.3390/ma17194797.

[62] K.E.K. Vimal, S. Vinodh, A. Raja, Modelling, assessment and deployment of strategies for ensuring sustainable shielded metal arc welding process – a case study, J. Clean. Prod. 93 (2015) 364–377, https://doi.org/10.1016/j.jclepro.2015.01.049.

[63] Y. Ding, X. Li, Z. Wang, C. Shen, M. Wang, N. Chen, L. Wang, W. Zhou, G. Ruan, Y. Cai, B. Qian, X. Hua, Comparative study of parallel gap resistance welding joints between different interconnected foils and GaAs solar cells: microstructure and thermal reliability, J. Manuf. Process. 109 (2024) 89–99, https://doi.org/10.1016/j.jmapro.2023.12.015.

[64] Fundamentals and Principles of Electrode-Position, in: Springer Series in Surface Sciences, Springer International Publishing, Cham, 2017, pp. 75–121, https://doi.org/10.1007/978-3-319-44920-3_3.

[65] A01 Committee, Practice for Cleaning, Descaling, and Passivation of Stainless Steel Parts, Equipment, and Systems, (n.d.). https://doi.org/10.1520/A0380_A0380M-17.
[66] S. Gong, F. Wang, K. Chen, AlN and Nb(C,N) composite precipitation behaviors and their effects on austenite grain growth in SCr420H high-temperature carburized gear steel, Steel Res. Int 95 (2024), https://doi.org/10.1002/srin.202400080.
[67] O.S.I. Fayomi, I.G. Akanade, A.A. Sode, A review on the efficacy of electroplating in deteriorating environments, J. Phys. Conf. Ser. 1378 (2019) 042084, https://doi.org/10.1088/1742-6596/1378/4/042084.
[68] Introduction to Electrodeposition: Basic Terms and Fundamental Concepts, in: Theory and Practice of Metal Electrodeposition, Springer New York, New York, NY, 2011: pp. 1–25. https://doi.org/10.1007/978-1-4419-9669-5_1.
[69] Z. Wang, P. Xiao, J. Shemilt, Fabrication of composite coatings using a combination of electrochemical methods and reaction bonding process, J. Eur. Ceram. Soc. 20 (2000) 1469–1473, https://doi.org/10.1016/s0955-2219(00)00034-0.
[70] F.C. Walsh, S. Wang, N. Zhou, The electrodeposition of composite coatings: diversity, applications and challenges, Curr. Opin. Electrochem. 20 (2020) 8–19, https://doi.org/10.1016/j.coelec.2020.01.011.
[71] J.O. Iroh, Y. Zhu, K. Shah, K. Levine, R. Rajagopalan, T. Uyar, M. Donley, R. Mantz, J. Johnson, N.N. Voevodin, V.N. Balbyshev, A.N. Khramov, Electrochemical synthesis: a novel technique for processing multi-functional coatings, Prog. Org. Coat. 47 (2003) 365–375, https://doi.org/10.1016/j.porgcoat.2003.07.006.
[72] G. İrsel, Study of the microstructure and mechanical property relationships of shielded metal arc and TIG welded S235JR steel joints, Materials Science Engineering A 830 (2022) 142320, https://doi.org/10.1016/j.msea.2021.142320.
[73] G. Shit, M.V. Kuppusamy, S. Ningshen, Corrosion Resistance Behavior of GTAW Welded AISI type 304L Stainless Steel, Trans. Indian Inst. Met 72 (2019) 2981–2995, https://doi.org/10.1007/s12666-019-01779-w.
[74] M. Elmas, O. Koçar, N. Anaç, Study of the Microstructure and Mechanical Property Relationships of Gas Metal Arc Welded Dissimilar Protection 600T, DP450 and S275JR Steel Joints, Crystals 14 (2024) 477, https://doi.org/10.3390/cryst14050477.
[75] ASTM E8/E8M-21, Standard Test Methods for Tension Testing of Metallic Materials, (2022). ⟨https://store.astm.org/e0008_e0008m-21.html⟩ (accessed May 1, 2025).
[76] Série HMV-G - Características, (n.d.). ⟨https://www.shimadzu.com.br/analitica/produtos/teste-de-materiais/ensaio-de-dureza/serie-hmv-g/features.html⟩ (accessed May 1, 2025).
[77] T. Reza Tabrizi, M. Sabzi, S.H. Mousavi Anijdan, A.R. Eivani, N. Park, H. R. Jafarian, Comparing the effect of continuous and pulsed current in the GTAW process of AISI 316L stainless steel welded joint: microstructural evolution, phase equilibrium, mechanical properties and fracture mode, J. Mater. Res. Technol. 15 (2021) 199–212, https://doi.org/10.1016/j.jmrt.2021.07.154.
[78] A. D, T. R, Investigations on microstructural characteristics and mechanical properties of 316 L stainless steel welded joints using nickel-coated filler material by gas tungsten arc welding, Mater. Res. Express 8 (2021) 046513, https://doi.org/10.1088/2053-1591/abf3e7.
[79] E04 Committee, Test Method for Determining Volume Fraction by Systematic Manual Point Count, (n.d.). https://doi.org/10.1520/e0562-19e01.
[80] M.D. Asaduzzaman, C. Mohammad, I. Mayeedul, Effects of concentration of sodium chloride solution on the pitting corrosion behavior of AISI 304L austenitic stainless steel, CICEQ 17 (2011) 477–483, https://doi.org/10.2298/CICEQ110406032A.
[81] E04 Committee, Test Method for Determining Volume Fraction by Systematic Manual Point Count, (n.d.). https://doi.org/10.1520/E0562-19E01.
[82] G01 Committee, ASTM G5-14(2021), Reference Test Method for Making Potentiodynamic Anodic Polarization Measurements, (n.d.). https://doi.org/10.1520/G0005-14R21.
[83] G01 Committee, ASTM G59–23, Test Method for Conducting Potentiodynamic Polarization Resistance Measurements, (n.d.). https://doi.org/10.1520/G0059-23.
[84] Elsevier, 2021, https://doi.org/10.1016/C2018-0-01137-8.
[85] S. Wolynec, Técnicas eletroquímicas em corrosão, EDUSP São Paulo (2003).
[86] O. Ambrož, J. Čermák, P. Jozefovič, Š. Mikmeková, Effects of etchant stirring on the surface quality of the metallography sample, J. Phys. Conf. Ser. 2572 (2023) 012011, https://doi.org/10.1088/1742-6596/2572/1/012011.
[87] Thermo-Calc Software v. 2024b Now Available, Thermo-Calc Software (2024). ⟨https://thermocalc.com/blog/thermo-calc-2024b-release-overview/⟩ (accessed August 11, 2025).
[88] J. Dykas, L. Samek, A. Grajcar, A. Kozłowska, Modelling of phase diagrams and continuous cooling transformation diagrams of medium manganese steels, Symmetry 15 (2023) 381, https://doi.org/10.3390/sym15020381.
[89] C.D. Cirstea, E. Povoden-Karadeniz, V. Cirstea, F. Tolea, E. Kozeschnik, Thermodynamic and kinetic simulations used for the study of the influence of precipitates on thermophysical properties in NiTiCu alloys obtained by spark plasma sintering, Nanomaterials 14 (2024) 461, https://doi.org/10.3390/nano14050461.
[90] R. Hu, G. Bai, J. Li, J. Zhang, T. Zhang, H. Fu, Precipitation behavior of grain boundary M23C6 and its effect on tensile properties of Ni–Cr–W based superalloy, Mater. Sci. Eng. A 548 (2012) 83–88, https://doi.org/10.1016/j.msea.2012.03.092.
[91] Y. Suwa, Y. Saito, Computer simulation of grain growth by the phase field model. effect of interfacial energy on kinetics of grain growth, Mater. Trans. 44 (2003) 2245–2251, https://doi.org/10.2320/matertrans.44.2245.
[92] D. Ye, L. Xiao, H. Cha, P. Xu, Y. Xu, Use of instrumented micro-indentation to study the mesoscopic elasto-plastic behavior of GH4145/SQ superalloy during high-temperature cyclic straining, Mater. Sci. Eng. A 528 (2011) 6825–6837, https://doi.org/10.1016/j.msea.2011.05.033.
[93] Matplotlib — Visualization with Python, (n.d.). ⟨https://matplotlib.org/⟩ (accessed August 11, 2025).
[94] D.J.Kotecki Lippold, Welding metallurgy and weldability of stainless steels, Wiley-VCH, Hoboken (N. J.), 2005.
[95] Y.H. Kim, D.J. Lee, J.C. Byun, et al., The effect of sigma phases formation depending on Cr/Ni equivalent ratio in AISI 316L weldments, Mater. Des. 32 (2011) 330–336, https://doi.org/10.1016/j.matdes.2010.06.044.
[96] H.-Y. Chu, R.-K. Shiue, S.-Y. Cheng, The effect of homogenization heat treatment on 316L stainless steel cast billet, Materials 17 (2023) 232, https://doi.org/10.3390/ma17010232.
[97] Y. Wang, C. Chen, X. Yang, Z. Zhang, J. Wang, Z. Li, L. Chen, W. Mu, Solidification modes and delta-ferrite of two types of 316L stainless steels: a combination of as-cast microstructure and HT-CLSM research, J. Iron Steel Res. Int. 32 (2025) 426–436, https://doi.org/10.1007/s42243-024-01401-4.